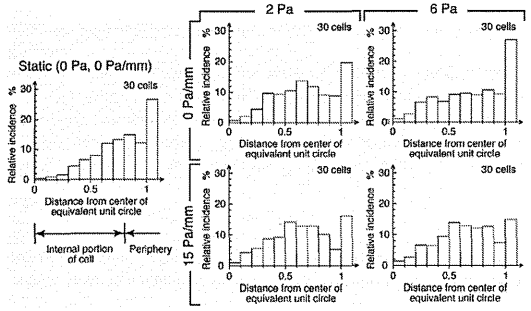

Fig. 5 Relative incidence of paxillin from the viewpoint of distance from the center of equivalent unit circle that indicates the EC outline.

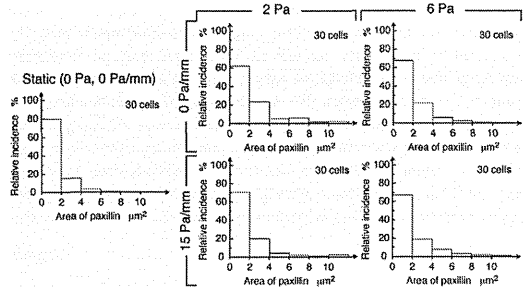

Fig. 6 Relative incidence of paxillin focusing on expression area of paxillin.

ECs exposed to SS without SSG was localized in the cell periphery. On closer inspection, paxillin was expressed in upstream and downstream in flow. ECs exposed to SS with SSG had the tendency to express paxillin not only in the periphery but also in the interior portion.

Tendency in areas of the expressed paxillin was similar, regardless of whether ECs were exposed to SS with or without spatial gradient. The areas of paxillin in the cells exposed to flow tended to increase in comparison with static condition, as illustrated in Fig. 6. Under the static condition, ECs had little expression of paxillin with area of more than 6 μm^2. Focusing on paxillin with the large area, namely the area is larger than 6 μm^2, we evaluated localization of the paxillin in the cell (Fig. 7). When ECs were exposed to SS with no spatial gradient, the paxillin with large area was commonly expressed in the cell periphery. In contrast, the cells exposed to flow with spatial gradient had a tendency to express the large paxillin in the interior portion.

5. Discussion

In the present study, we developed the D chamber that can generate uniform spatial SS gradient to evaluate effects of SSG itself on the cell morphology. The performance about linear increase in SS, namely constant SSG, was confirmed based on the CFD simulations.

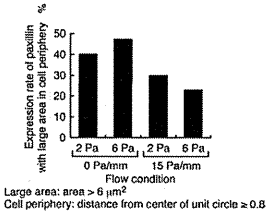

Fig.7 Expression rate of paxillin with large area (> 6 μm^2) in cell periphery (distance from the center of unit circle ≥ 0.8).

Although Dolan et al. [8] manufactured the flow chamber with the channel similar to the D chamber, local increase in SSG and spike in SS were observed in upstream and downstream sides, respectively, and they could not generate the constant SSG condition. These problems were not found in our flow chamber. Difference in pressure between upstream and downstream in flow chamber was up to 3 kPa (22.5 mmHg). Because this pressure value is lower than that in the previous studies about responses of ECs to hydrostatic pressure [14, 15], pressure is considered to have an insignificant effect on the cell morphology in the present experiments.

We clearly found the effect of combined SS and uniform SSG on EC response to fluid flow. After exposure to SS without spatial gradient for 24 hours, ECs elongated and oriented in the direction of flow. Actin filaments in the cell periphery developed and became thick along the direction of flow. In contrast, cells did not show obvious elongation, orientation, and development of thick actin filaments under the condition of SS with uniform SSG. Instead, thin and short filaments formed in the interior portion of the EC. The results in the present study correspond to the report of endothelial morphological responses under the combination of SS and variable SSG [7]. Intracellular signaling activated by SSG may inhibit the formation and development of thick actin filaments. As a result, it is considered that thin and short filaments formed in the interior portion of the EC. Therefore, these results suggest that cytoskeletal structures changed in response to the spatial gradient of SS.

Many studies have reported the mechanisms about sensing and converting SS into intracellular biochemical signals. Focal adhesion complex [16], platelet-endothelial cellular adhesion molecules (PECAM)-1 [17] are now thought as mechano-sensing molecules to SS. On the other hand, several studies have reported that difference in forces acting on intercellular junctions between the neighboring ECs along the direction of flow is important for sensing SSG. Ueki et al. [18] have found that tensile force applied to intercellular junctions by using a microneedle causes recruitment of activated Src homology 2-containig tyrosine phosphatase-2 (SHP-2) binding to an intercellular adhesion molecule PECAM-1. This result suggests that ECs can sense SSG if SSG causes difference in forces on cell junctions. However, force acting on intercellular junctions by flow exposure is considered to be much smaller than that in the direct tensile experiment by the microneedle. In addition, because changes in SSG exists in the flow channel of T-chamber used in previous studies, big difference in forces acting on cell junction may occur in comparison with the condition of uniform SSG. When effects of SSG pure and simple on ECs' morphology are evaluated, difference in forces on a cell junction can contribute less to sensing of SSG. In this study, we thus focused on paxillin, which is a focal adhesion-associated protein. Under the condition of SS without SSG, paxillin localized in the periphery of the EC, and aggregation of paxillin occurred in relatively large numbers in the cell periphery. The previous studies have also reported that SS provoked disaggregation and redistribution of

focal adhesion in the interior portion of a cell, and focal adhesion localized in the cell periphery [19]. However, paxillin was expressed not only in the cell periphery but also in the interior portion of the cell in the EC exposed to SS with its uniform SSG. Aggregation of paxillin tended to occur more commonly in the interior portion of the cell. Therefore, the spatial gradient of SS could inhibit redistribution of focal adhesion.

Endothelial cells are known to regulate cell migration and focal adhesion turnover by phosphorylation of 31st tyrosine residue to N-terminal (Tyr31) in paxillin [20]. When ECs, into which paxillin Y31A mutants were introduced, were exposed to SS of 1.2 Pa for 12 hours, paxillin Y31A mutants did not localize in the cell periphery and were distributed in the cell interior [20]. It was suggested that paxillin in ECs exposed to SS was not redistributed and did not aggregate in the cell periphery by inhibiting phosphorylation of Tyr31 in paxillin. This phenomenon is similar to distributions of paxillin in ECs under the condition of SS with uniform SSG. Therefore, SSG could have the potential to inhibit phosphorylation of Tyr31 in paxillin. Alternatively, SSG might be considered to suppress activation of FAK or proto-oncogene tyrosine-protein kinase Src, which cause phosphorylation of Tyr31 in paxillin [21].

The spatial gradient of SS has an important role in suppressing development of actin filaments and redistribution of focal adhesion, which are associated with morphological changes in ECs. However, it still remains unclear whether signal transduction of SSG via focal adhesion or intercellular adhesion molecules dominantly acts on endothelial morphology. The detail about signal transduction of SSG will be investigated in future studies.

6. Conclusion

In the present study, we developed the novel flow chamber to evaluate effects of SSG on morphological responses of ECs to fluid flow. ECs' responses to the combination of SS and uniform SSG were investigated using the developed chamber. ECs maintained a confluent monolayer under SS of 2 and 6 Pa with SSG of 0 and 15 Pa/mm. ECs elongated and aligned parallel to the direction of flow with development of thick actin filaments and localization of paxillin in the cell periphery after exposure to SS without SSG for 24 hours. In contrast, the ECs exposed to SS with SSG did not elongate and orient in the direction of flow, development of thick actin filaments and the localization of paxillin were not confirmed. These results suggested that SSG suppresses formations of actin filaments and redistribution of focal adhesion, resulting in the inhibition of EC morphological changes in response to flow.

Acknowledgment

The present study was supported in part by Grants-in-Aid for Scientific Research from the Ministry of Education, Culture, Sports, Science and Technology (MEXT) of Japan (No. 20001007).

References

(1) Kataoka, N., Ujita, S., Kimura, K. and Sato, M., The morphological responses of cultured bovine aortic endothelial cells to fluid-imposed shear stress under sparse and colony conditions, *JSME International Journal, Series C*, Vol.41, No.1 (1998), pp.76–82.
(2) Malek, A. M., Alper, S. L. and Izumo, S., Hemodynamic shear stress and its role in atherosclerosis, *Journal of the American Medical Association*, Vol.282, No.21 (1999), pp.2035–2042.
(3) Davies, P. F., Flow-mediated endothelial mechanotransduction, *Physiological Reviews*, Vol.75, No.3 (1995), pp.519–560.
(4) Sato, M., Suzuki, K., Ueki, Y. and Ohashi, T., Microelastic mapping of living endothelial cells exposed to shear stress in relation to three-dimensional distribution of actin filaments, *Acta Biomaterialia*, Vol.3, No.3 (2007), pp.311–319.
(5) Zaidel-Bar, R., Kam, Z. and Geiger, B., Polarized downregulation of the paxillin-p130CAS-Rac1 pathway induced by shear flow, *Journal of Cell Science*, Vol.118, No.17 (2005), pp. 3997–4007.
(6) Szymanski, M. P., Metaxa, E., Meng, H. and Kolega, J., Endothelial cell layer subjected to impinging flow mimicking the apex of an arterial bifurcation, *Annals of Biomedical Engineering*, Vol.36, No.10 (2008), pp.1681–1689.
(7) Sakamoto, N., Saito, N., Han, X., Ohashi, T. and Sato, M., Effect of spatial gradient in fluid shear stress on morphological changes in endothelial cells in response to flow, *Biochemical and Biophysical Research Communications*, Vol.395, No.2 (2010), pp.264–269.
(8) Dolan, J. M., Meng, H., Singh, S., Paluch, R. and Kolega, J., High fluid shear stress and spatial shear stress gradients affect endothelial proliferation, survival, and alignment, *Annals of Biomedical Engineering*, Vol.39, No.6 (2011), pp.1620–1631.
(9) Bacabac, R. G., Smit, T. H., Cowin, S. C., Van Loon, J. J., Nieuwstadt, F. T., Heethaar, R. and Klein-Nulend, J., Dynamic shear stress in parallel-plate flow chambers, *Journal of Biomechanics*, Vol.38, No.1 (2005), pp.159–167.
(10) Meng, H., Wang, Z., Hoi, Y., Gao, L., Metaxa, E., Swartz D. D. and Kolega, J., Complex hemodynamics at the apex of an arterial bifurcation induces vascular remodeling resembling cerebral aneurysm initiation, *Stroke*, Vol.38, No.6 (2007), pp.1924–1931.
(11) Sakamoto, N., Ohashi, T. and Sato, M., Effect of magnetic field on nitric oxide synthesis of cultured endothelial cells, *International Journal of Applied Electromagnetics and Mechanics*, Vol.14, No.1-4 (2002), pp.317–322.
(12) Oshima, M., Image-based simulation of blood flow for cerebrovascular disorders, *Journal of Japan Society of Fluid Mechanics*, Vol.21, No.2 (2002), pp.122–128.
(13) Castro, M. A., Putman, C. M., Sheridan, M. J. and Cebral, J. R., Hemodynamic patterns of anterior communicating artery aneurysms: a possible association with rupture, *American journal of neuroradiology*, Vol.30, No.2 (2009), pp.297–302.
(14) Ohashi, T., Sugaya, Y., Sakamoto, N. and Sato, M., Hydrostatic pressure influences morphology and expression of VE-cadherin of vascular endothelial cells, *Journal of Biomechanics*, Vol.40, No.11 (2007), pp.2399–405
(15) Müller-Marschhausen, K., Waschke, J. and Drenckhahn, D., Physiological hydrostatic pressure protects endothelial monolayer integrity, *American Journal of Physiology. Cell Physiology*, Vol.294, No.1 (2008), pp.C324–C332.
(16) Wang, Y., Miao, H., Li, S., Chen, K. D., Li, Y. S., Yuan, S., Shyy, J. Y. and Chien, S., Interplay between integrins and FLK-1 in shear stress-induced signaling, *American journal of physiology. Cell physiology*, Vol.283, No.5 (2002), pp.C1540–C1547.
(17) Tzima, E., Irani-Tehrani, M., Kiosses, W. B., Dejana, E., Schultz, D. A., Engelhardt, B., Cao, G, DeLisser, H. and Schwartz, M. A., A mechanosensory complex that mediates the endothelial cell response to fluid shear stress, *Nature*, Vol.437, No.7057 (2005), pp.426–431.
(18) Ueki, Y., Sakamoto, N., Ohashi, T. and Sato, M., Morphological responses of vascular endothelial cells induced by local stretch transmitted through intercellular junctions, *Experimental Mechanics*, Vol.49, No.1 (2009), pp.125-134.
(19) Li, S., Butler, P., Wang, Y., Hu, Y., Han, D., Usami, S., Guan, J. and Chien, S., The role of the dynamics of focal adhesion kinase in the mechanotaxis of endothelial cells, *Proceedings of the National Academy of Sciences of the United States of America*, Vol.99, No.6 (2002), pp.3546–3551.
(20) Mattiussi, S., Matsumoto, K., Illi, B., Martelli, F., Capogrossi, M. C. and Gaetano, C.,

Papilloma protein E6 abrogates shear stress-dependent survival in human endothelial cells: Evidence for specialized functions of paxillin, *Cardiovascular Research*, Vol.70, No.3 (2006), pp.578–588.

(21) Brown, M. C. and Turner, C. E., Paxillin: adapting to change, *Physiological Reviews*, Vol.84, No.4 (2004), pp.1315–1339.

Ultrasound Obstet Gynecol 2013; 42: 112–114
Published online in Wiley Online Library (wileyonlinelibrary.com). DOI: 10.1002/uog.12466

First successful case of non-invasive *in-utero* treatment of twin reversed arterial perfusion sequence by high-intensity focused ultrasound

T. OKAI*, K. ICHIZUKA*, J. HASEGAWA*, R. MATSUOKA*, M. NAKAMURA*, K. SHIMODAIRA*, A. SEKIZAWA*, M. KUSHIMA† and S. UMEMURA‡

**Department of Obstetrics and Gynecology, School of Medicine, Showa University, Tokyo, Japan; †Department of Pathology, School of Medicine, Showa University, Tokyo, Japan; ‡Graduate School of Biomedical Engineering, Tohoku University, Sendai, Japan*

KEYWORDS: fetal therapy; HIFU; TRAP sequence

ABSTRACT

High-intensity focused ultrasound (HIFU) has excellent potential as a non-invasive therapeutic tool in various fields of medicine. We present a case of twin reversed arterial perfusion sequence, in which non-invasive blood flow occlusion in the acardiac fetus was successfully achieved by means of HIFU exposure from outside the maternal abdomen. HIFU was applied to blood vessels of the acardiac fetus at the point at which the umbilical cord entered the body in a series of four procedures at 3-day intervals starting at 13 weeks' gestation, and in a final procedure with higher power at 17 weeks. The HIFU intensity was set at approximately 2300 W/cm² for the initial series of procedures and at 4600 W/cm² for the final procedure, with exposure periods of 10 s. As color Doppler examination revealed absence of blood flow to the acardiac fetus after the second round of HIFU exposure, we concluded that complete occlusion of target vessels had been achieved. Delivery was by Cesarean section at 37 weeks' gestation. A male neonate (the pump fetus) was born weighing 1903 g with Apgar scores of 8 and 9 at 1 and 5 min, respectively. At the time of writing, the baby was healthy and growing normally, with the exception of congenital pseudarthrosis. Copyright © 2013 ISUOG. Published by John Wiley & Sons Ltd.

CASE REPORT

A 32-year-old woman, gravida 1 para 0, who was pregnant with twins, was referred to our hospital because of the absence of a heart beat in one fetus. Based on the ultrasonographic findings, we diagnosed twin reversed arterial perfusion (TRAP) sequence. Following ethics committee approval and counseling of the patient, which included a thorough explanation of the procedure as well as the possible adverse effects on the mother and pump fetus and the results of our previous case[1], we conducted high-intensity focused ultrasound (HIFU) treatment (Figure 1). The aim of HIFU was to non-invasively occlude blood flow in the acardiac fetus with the aim of diminishing the cardiac burden in the normal 'pump' fetus.

The HIFU transducer used in this case was a prototype developed by us with a resonant frequency of 1.71 MHz, a spherical radius of curvature of 60 mm, and a focal length of 60 mm. The exposure method and conditions were derived from the findings of our previous animal experiments[2,3] and the first clinical case[1]. The blood vessel of the acardiac fetus at the point at which the umbilical cord entered the body was targeted for HIFU exposure through the maternal abdomen.

HIFU irradiation was conducted at 13 + 5 weeks' gestation. The HIFU intensity at the focused area (3.6 mm²) was set at approximately 2300 W/cm² with exposure times of 10 s repeated several times. Following this first round of irradiation, blood flow in the aorta of the acardiac fetus became very weak. However, the following day blood flow had recovered to its preoperative state (Figure 2a). The patient did not suffer any adverse events from the procedure, and she opted for a series of repeat procedures. We conducted three more courses of HIFU exposure in a similar manner at 3-day intervals. However, the results were similar to that of the first procedure. At 17 + 5 weeks' gestation, we decided to increase the emission power of the HIFU and performed the procedure at a higher power of 4600 W/cm². This resulted in cessation of blood flow in the acardiac fetus and its umbilicus the following day, indicating complete occlusion (Figure 2b).

Correspondence to: Dr K. Ichizuka, Showa University, School of Medicine, Department of Obstetrics and Gynecology, 142–8666 Hatanodai, Shinagawa-ku, Tokyo, Japan (e-mail: k.ichizuka@me.com)

Accepted: 14 March 2013

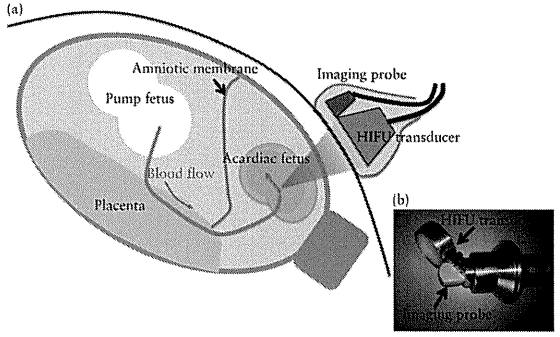

Figure 1 (a) Schematic diagram showing application of high-intensity focused ultrasound (HIFU) in a case of twin reversed arterial perfusion sequence and (b) photograph of HIFU transducer and imaging probe, which were applied after placing in a plastic bag filled with degassed water.

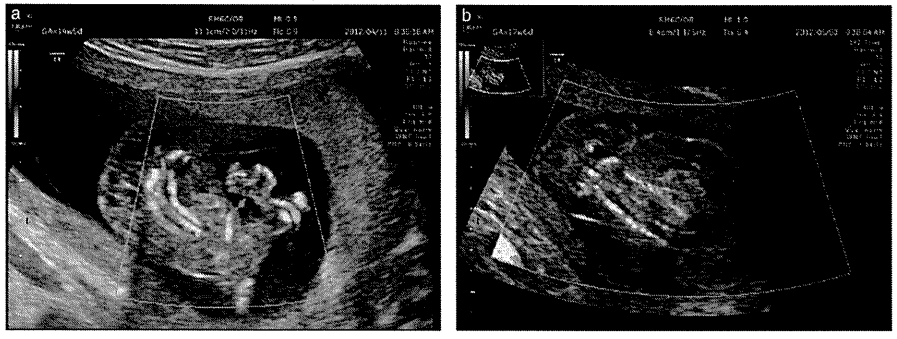

Figure 2 Color Doppler ultrasound images of acardiac fetus at 14 + 5 weeks' gestation, after initial series of high-intensity focused ultrasound (HIFU) procedures (a) and at 17 weeks' gestation, after final HIFU procedure (b).

The patient did not exhibit any signs or symptoms of threatened premature labor, such as uterine contractions or dilation of the cervix, either during or following the procedure. Furthermore, the pump fetus did not exhibit any abnormal behavior and its heart rate and umbilical blood flow did not vary. However, at 28 weeks' gestation the fetus appeared small for gestational age, indicating fetal growth restriction. At 37 weeks' gestation, an emergency Cesarean section was performed owing to a rapid increase in the patient's blood pressure (170/100 mmHg). A male neonate was born weighing 1903 g with Apgar scores of 8 and 9 at 1 and 5 min, respectively. We performed the auditory brainstem response test, which confirmed that the auditory function of the neonate was intact. Congenital pseudarthrosis of the left leg was later diagnosed by an orthopedist, but other than this the neonate was healthy and was discharged without any other abnormalities.

The length of the acardiac fetus was 5.5 cm (Figure 3). It had a shrunken and macerated appearance with tissue degeneration. The cord was not visible at the time of delivery, so we could not obtain macroscopic or histological findings of the site targeted by HIFU irradiation.

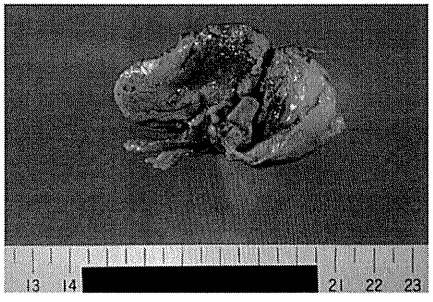

Figure 3 Postdelivery photograph of acardiac fetus.

DISCUSSION

This is the first case in which HIFU treatment has been successfully conducted on a human fetus. Through previously conducted animal experiments[2,3], we identified TRAP sequence as the most suitable fetal disorder for *in-utero* treatment with HIFU.

Recently, TRAP sequence has been treated using radiofrequency ablation therapy[4,5], which is less invasive than the endoscopic technique that has been applied in the past[6,7]. However, because of the insertion of devices into the uterus, the radiofrequency ablation procedure is associated with a risk of hemorrhage, rupture of membranes and premature birth. In contrast, HIFU treatment is a non-invasive procedure that uses external ultrasound waves that can be transmitted through solid tissue and focused within the body to destroy deep target tissues. It has been proven through animal experiments that HIFU enables thermal denaturation of fetal blood vessels *without direct fetal contact*[3].

Irradiation treatment with HIFU at 13 weeks' gestation did not increase the temperature of the fetal blood vessel wall adequately to accomplish occlusion of blood flow. This result was probably due to inadequate ultrasound intensity at the focal point. In previous animal experiments, adequate ultrasound intensity at the focal point was obtained when the transducer output was 100 W with 83% transfer efficiency[3]. However the same intensity would not have been achieved in a human patient owing to attenuation of ultrasound power that would occur as it passes through the subcutaneous fat layer, which is thinner in experimental animals. Therefore, we increased the emitting electrical power to 200 W, as previously tested in animal experiments, in which a greater ultrasound intensity had been successfully obtained. The intensity at the focal point was theoretically 4600 W/cm^2 without considering any attenuation, achieving complete occlusion of blood flow in the acardiac fetus. Following this successful experience, we will consider higher HIFU intensities at the initial irradiation treatment in future cases.

Compared with conventional therapy for TRAP sequence, the advantage of HIFU is that it does not cause injury to the mother or the uterus, except after a long irradiation time. In this instance, the patient experienced abdominal warmth and lower back pain when the focused and widened HIFU beam hit the lumbar vertebrae. Therefore, as long as we can control levels of abdominal warmth and the direction of the ultrasound beam, we can treat TRAP sequence non-invasively by HIFU.

It is difficult to determine whether HIFU exposure was associated with the neonate's pseudarthrosis of the leg. Although in this case the cause of this disease is unknown, there is a well-known relationship between congenital pseudarthrosis and neurofibramotosis type 1, an autosomal dominant disease[8]. In this case, there were no other affected individuals in the family. We think it is likely that the condition arose spontaneously, because the acoustic window did not include the pump fetus; that is, the HIFU beam did not pass through the pump fetus, including the left limb. We also do not believe that there is any association between the HIFU procedure and the occurrence of pregnancy-induced hypertension and fetal growth restriction seen in this case because placental pathology revealed no sign of the typical lesions often induced by HIFU exposure, and the HIFU beam did not pass through the placenta. At last follow-up the neonate was healthy, excluding pseudarthrosis of the left leg. However, long-term neurodevelopmental outcome after fetal therapy cannot yet be assessed[9], therefore further follow-up of this case over a long period of time is necessary.

The present case adds a new possible modality for non-invasive *in-utero* treatment of TRAP sequence.

REFERENCES

1. Ichizuka K, Hasegawa J, Nakamura M, Matsuoka R, Sekizawa A, Okai T, Umemura S. High-intensity focused ultrasound treatment for twin reversed arterial perfusion sequence. *Ultrasound Obstet Gynecol* 2012; 40: 476–478.
2. Ishikawa T, Okai T, Sasaki K, Umemura S, Fujiwara R, Kushima M, Ichihara M, Ichizuka K. Functional and histological changes in rat femoral arteries by HIFU exposure. *Ultrasound Med Biol* 2003; 29: 1471–1477.
3. Ichizuka K, Ando S, Ichihara M, Ishikawa T, Uchiyama N, Sasaki K, Umemura S, Matsuoka R, Sekizawa A, Okai T. Application of high-intensity focused ultrasound for umbilical artery occlusion in a rabbit model. *Ultrasound Obstet Gynecol* 2007; 30: 47–51.
4. Tsao K, Feldstein VA, Albanese CT, Sandberg PL, Lee H, Harrison MR, Farmer DL. Selective reduction of acardiac twin by radiofrequency ablation. *Am J Obstet Gynecol* 2002; 187: 635–640.
5. Bebbington MW, Danzer E, Moldenhauer J, Khalek N, Johnson MP. Radiofrequency ablation vs bipolar umbilical cord coagulation in the management of complex monochorionic pregnancies. *Ultrasound Obstet Gynecol* 2012; 40: 319–324.
6. Hecher K, Lewi L, Gratacos E, Huber A, Ville Y, Deprest J. Twin reversed arterial perfusion: fetoscopic laser coagulation of placental anastomoses or the umbilical cord. *Ultrasound Obstet Gynecol* 2006; 28: 688–691.
7. Nakata M, Sumie M, Murata S, Miwa I, Matsubara M, Sugino N. Fetoscopic laser photocoagulation of placental communicating vessels for twin-reversed arterial perfusion sequence. *J Obstet Gynaecol Res* 2008; 34: 649–652.
8. Pannier S. Congenital pseudarthrosis of the tibia. *Orthop Traumatol Surg Res* 2011; 97: 750–761.
9. van Klink JM, Koopman HM, Oepkes D, Walther FJ, Lopriore E. Long-term neurodevelopmental outcome in monochorionic twins after fetal therapy. *Early Hum Dev* 2011; 87: 601–606.

Relative Residence Time Prolongation in Intracranial Aneurysms: A Possible Association With Atherosclerosis

Shin-ichiro Sugiyama, MD*‡
Kuniyasu Niizuma, MD*
Toshio Nakayama, PhD§
Hiroaki Shimizu, MD¶
Hidenori Endo, MD¶
Takashi Inoue, MD¶
Miki Fujimura, MD‖
Makoto Ohta, PhD#
Akira Takahashi, MD§
Teiji Tominaga, MD*

*Department of Neurosurgery, Tohoku University Graduate School of Medicine, Sendai, Japan; ‡Department of Neuroanesthesia, and ¶Department of Neurosurgery, Kohnan Hospital, Sendai, Japan; §Graduate School of Biomedical Engineering, and #Institute of Fluid Science, Tohoku University, Sendai, Japan; ‖Department of Neurosurgery, Sendai Medical Center, Sendai, Japan

Correspondence:
Kuniyasu Niizuma, MD, PhD,
Department of Neurosurgery,
Tohoku University
Graduate School of Medicine,
1-1 Seiryo-machi, Aoba-ku, Sendai,
Miyagi 980-8574, Japan.
E-mail: niizuma@nsg.med.tohoku.ac.jp

Received, September 27, 2012.
Accepted, July 10, 2013.
Published Online, July 16, 2013.

WHAT IS THIS BOX?
A QR Code is a matrix barcode readable by QR scanners, mobile phones with cameras, and smartphones. **The QR Code above links to Supplemental Digital Content from this article.**

BACKGROUND: Intracranial aneurysms can have atherosclerotic wall properties that may be important in predicting aneurysm history or estimating the potential risks of surgical treatments.
OBJECTIVE: To investigate hemodynamic characteristics of atherosclerotic lesions in intracranial aneurysms using computational fluid dynamics.
METHODS: Intraoperative video recordings of 30 consecutive patients with an unruptured middle cerebral artery aneurysm were examined to identify atherosclerotic lesions on an aneurysm wall. For computational fluid dynamics analyses, geometries of aneurysms and adjacent arteries were reconstructed from 3-dimensional rotational angiography. Transient simulations were conducted under patient-specific pulsatile inlet conditions measured by phase-contrast magnetic resonance velocimetry. Three hemodynamic wall parameters were calculated: time-averaged wall shear stress, oscillatory shear index, and relative residence time (RRT). Statistical analyses were performed to discriminate the risk factors of atherosclerotic lesion formation.
RESULTS: Among 30 aneurysms, 7 atherosclerotic lesions with remarkable yellow lipid deposition were identified in 5 aneurysms. All 7 atherosclerotic lesions spatially agreed with the area with prolonged RRT. Univariate analysis revealed that male sex ($P = .03$), cigarette smoking ($P = .047$), and maximum RRT ($P = .02$) are significantly related to atherosclerotic lesion on the intracranial aneurysmal wall. Of those variables that influenced atherosclerotic lesion of the intracranial aneurysmal wall, male sex ($P = .005$) and maximum RRT ($P = .004$) remained significant in the multivariate regression model.
CONCLUSION: The area with prolonged RRT colocalized with atherosclerotic change on the aneurysm wall. Male sex and maximum RRT were independent risk factors for atherogenesis in intracranial aneurysms.

KEY WORDS: Atherosclerosis, Cerebral aneurysm, Hemodynamics, Oscillatory shear stress, Relative residence time, Wall shear stress

Neurosurgery 73:767–776, 2013 DOI: 10.1227/NEU.0000000000000096 www.neurosurgery-online.com

With recent advances in diagnostic neuroradiological imaging, many unruptured intracranial aneurysms have been discovered. Several large prospective studies showed that some morphological factors such as size, location, and irregular shape might help to predict the risk for rupture of unruptured aneurysms.[1,2] However, biomechanical reasons underlying these morphological risk factors remain unclear. The morphology of an aneurysm has a definite influence on the hemodynamics inside that aneurysm. Therefore, recent studies have investigated the relation between aneurysm geometry and hemodynamics and the role of this relation in the natural history of intracranial aneurysms.[3,4]

ABBREVIATIONS: CFD, computational fluid dynamics; **MCA,** middle cerebral artery; **OSI,** oscillatory shear index; **RRT,** relative residence time; **WSS,** wall shear stress

Supplemental digital content is available for this article. Direct URL citations appear in the printed text and are provided in the HTML and PDF versions of this article on the journal's Web site (www.neurosurgery-online.com).

Progress in computational fluid dynamics (CFD) has enabled hemodynamic simulation in realistic aneurysm geometries with increased accuracy and reliability.[5] In postvisualization of CFD simulation, blood flow inside aneurysms can be demonstrated using streamlines or velocity vector plots. In addition, the influence of intra-aneurysmal blood flow on the vascular wall can be characterized by hemodynamic wall parameters that are calculated from the results of CFD such as wall shear stress (WSS) and the oscillatory shear index (OSI). WSS is the tangential frictional stress caused by blood flow on the vascular wall. OSI is a dimensionless measure of directional changes in WSS and is used as a marker of the oscillatory nature of WSS.

These hemodynamic wall parameters are related to the biological processes on the aneurysm wall, and CFD simulations may be able to predict the rupture of intracranial aneurysms.[4,6-8] In particular, low WSS and high OSI have been proposed as indicators for the risk of aneurysm rupture.[4] Blood flow associated with such low or oscillatory WSS is generically considered a kind of disturbed blood flow,[9,10] although disturbed flow has many definitions. Aneurysm rupture may be driven by biological processes mediated by unphysiological WSS conditions, which have been shown to activate proinflammatory signaling pathways in endothelial cells.[11] Activation of such inflammatory pathways might cause degradation of the aneurysm wall and rupture of the aneurysms.[12,13]

On the other hand, low or oscillatory WSS is known to be a potential atherogenic stimulus in large arteries.[7,10,14] We previously reported a hemodynamic study of an intracranial aneurysm with atherosclerotic blebs that were subjected to low and oscillatory WSS.[15] These results suggest that such blood flow may have the potential to promote atherogenesis in intracranial aneurysms and in large arteries. Therefore, low or oscillatory WSS might cause different consequences, including rupture and atherogenesis. However, the mechanism or what triggers these different consequences is unknown. In particular, little work has been done on the atherosclerotic lesions of the intracranial aneurysms. The purpose of this study is to investigate the roles of hemodynamics on atherosclerosis in intracranial aneurysms. This knowledge may be important for estimating potential risks of surgery or in predicting the natural history of intracranial aneurysms.

We conducted CFD analysis of unruptured middle cerebral artery (MCA) aneurysms that were surgically treated and investigated the relation between the spatial distribution of atherosclerotic lesions on the aneurysm wall and hemodynamic wall parameters, including WSS and OSI. In addition to WSS and OSI, we calculated the relative residence time (RRT) introduced by Himburg et al[9] as a marker of low or oscillatory WSS. We also investigated intra-aneurysmal flow fields, which may be responsible for atherosclerosis in intracranial aneurysms.

PATIENTS AND METHODS

Patient Population

From October 2010 to September 2011, 30 unruptured MCA aneurysms were surgically treated at our hospital. All patients underwent 3-dimensional (3-D) rotational angiography and magnetic resonance (MR) examination, including velocity measurement of parent arteries, before the surgical treatment. Intraoperative video recordings were examined to distinguish atherosclerotic lesions on the aneurysm wall. This study was conducted in accordance with and under the approval of the ethics review board of our hospital.

Model Construction

Conventional digital subtraction and 3-D rotational angiography was performed by standard transfemoral catheterization with a biplane unit (Innova 3131; GE Healthcare Japan, Tokyo, Japan). These images were obtained during a 6-second injection of a contrast agent and a 200° rotation with imaging at 30 frames per second for 5 seconds. The 150 projection images were reconstructed into a 3-D data set of 512 × 512 × 512 isotropic voxels covering a field of view of 200 mm in all 3 directions.

The 3-D data set obtained from rotational angiography was exported to a personal computer to form a 3-D isosurface model of the aneurysms. The mean signal intensity of the parent artery (M1) was calculated and used as an initial threshold. A 3-D surface was extracted with the threshold using imaging software (Avizo 6.2; Visualization Science Group, Merignac, France). It was then displayed on the native axial, coronal, and sagittal slices of the original 3-D data set and adjusted until it visually matched the luminal boundary of all regions of interest. The results of segmentation were validated by 2-dimensional conventional angiograms in the anteroposterior and lateral views and intraoperative videograms of vessels and aneurysms exposed during surgery. The segmented 3-D surface was then processed with commercial software (Magics RP 13.1; Materialise, Leuven, Belgium) to smooth the fine irregularities, to make planes for inlets and outlets, and to clear small branches from the regions of interest. The rate of volume change was suppressed to ≤ 5% during the smoothing process. The data were output in a stereolithography format.

Quantitative MR Velocimetry

Quantitative MR velocimetry was performed with a 3-T MR image scanner (Signa HDxt; GE Healthcare Japan, Tokyo, Japan) before the surgical treatment. The protocol entails a standard cranial 3-D time-of-flight MR angiography to select a slice orientation for the arterial blood flow measurements. The optimal perpendicular scan plane was determined from the acquired time-of-flight images. The coordinates obtained specified the position of an oblique fast 2-dimensional phase-contrast sequence that was then performed on the basis of these coordinates using a peripheral gated 2-dimensional phase-contrast sequence with the following imaging parameters: repetition time/echo time/number of excitations, 25 milliseconds/5.4 milliseconds/1; field of view, 160 × 160 mm; matrix, 512 × 512; voxel size, 0.3 × 0.3 mm; velocity encoding, 100 cm/s; imaging time, about 5 minutes; direction, transaxial; peripheral gated with ECG; and phases, 30. The acquired phase-contrast images were transferred to the workstation for flow quantification with dedicated software (CV Flow; GE Healthcare Japan). A region of interest was placed semiautomatically on the phase-contrast images over a cardiac cycle. The velocities at all of the pixels inside the vessel border were integrated to calculate the flow in milliliters per second, and these values were used to obtain the quantitative waveform over the cardiac cycle (Figure 1).

Numerical Simulations

Each aneurysm model was meshed with the use of commercial software (ICEM CFD; ANSYS Inc, Lebanon, New Hampshire) to create tetrahedral meshes with 3 layers of finer-prism meshes in the boundary,

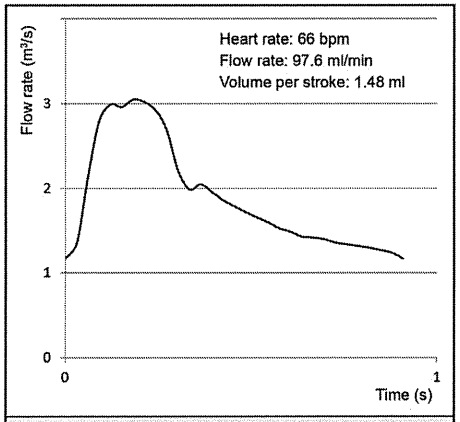

FIGURE 1. *An example of pulsatile waveform, heart rate, mean flow rate, and flow volume per stroke obtained from phase-contrast magnetic resonance velocimetry (case 2).*

resulting in approximately 1 million meshes. A finite-volume method package, ANSYS 12.1 (ANSYS Inc), was used to solve the governing equations: 3-D unsteady Navier-Stokes equations and equation of continuity. The patient-specific pulsatile-flow condition derived from the MR examinations was prescribed at the inlet boundary. The diffusion fluxes in the direction normal to the inlet plane were assumed to be zero, and normal gradients were neglected. Traction-free conditions (0 Pa) were substituted for outlets. Following the conventions for CFD in large vessels,[16] blood was modeled as an incompressible newtonian fluid with a density of 1050 kg/m^3 and a viscosity of 0.0035 kg/m·s. A rigid-wall no-slip boundary condition was implemented at the vessel walls. Three pulsatile cycles were simulated to ensure that numeric stability was reached, and the results from the third cycle were used for analysis.

Data Analysis

Three hemodynamic wall parameters including WSS, OSI, and RRT were calculated. Time-averaged WSS refers to the tangential frictional stress caused by the action of blood flow on the vessel wall. OSI is a dimensionless measure of directional changes in WSS to describe the temporal disturbance of intra-aneurysmal flow.[17] RRT demonstrates the residence time of particles near the wall, and RRT prolongation corresponds with low or oscillatory WSS.[9] These data were used to investigate the relation between the 3 parameters and atherosclerotic change of the aneurysms. Moreover, the maximum RRT, maximum OSI, and minimum WSS of each aneurysm were used for statistical analysis to find predictors of atherosclerosis in intracranial aneurysms. To visualize the flow field, 3-D streamlines of intra-aneurysmal flow and WSS vectors on the aneurysm wall over a cardiac cycle were plotted in the model with the use of commercial software (ANSYS CFD; Ansys Inc). Supplemental Digital Content 1 (http://links.lww.com/NEU/A577) gives a detailed description of WSS, OSI, and RRT.

An unpaired *t* test was used for parametric statistical analysis. Categorical variables were analyzed in contingency tables with the Fisher exact test. Results with values of $P < .05$ were considered statistically significant. In a second step, a multivariate analysis was performed to find independent predictors for the atherosclerotic lesions of the aneurysmal wall using a binary logistic regression analysis and to find confounding factors between potentially independent predictors. Variables with significant *P* values in univariate analyses were considered potentially independent variables in the multivariate analysis. A forward stepwise method was used to construct multivariate logistic regression models with the inclusion criterion of $P < .05$. All calculations were performed with standard commercial software (JMP Pro Version 9.02; SAS Institute Inc).

RESULTS

Intraoperative video recordings were examined for all 30 cases. The profiles of patients are listed in Table 1. Seven atherosclerotic lesions on 5 aneurysms (5 of 30, 16.7%) were distinguished by remarkable yellow lipid deposition. Five atherosclerotic lesions were located on the aneurysm dome, and 2 were located at the bleb. All 5 patients had several vascular atherosclerosis risk factors such as male sex, old age, obesity, smoking history, hypertension, diabetes mellitus, or dyslipidemia. MR velocimetry successfully measured the flow rate and flow volume per stroke of each patient (Figure 1). MR imaging indicated no thrombus in the aneurysms of all patients.

Among the 3 hemodynamic variables examined in the present study, only RRT demonstrated qualitative agreement with the spatial distribution of atherosclerosis in all 7 lesions as a single metric (Figures 2-4). All atherosclerotic lesions presented with high RRT and low WSS. The 5 lesions on the dome were exposed to low and oscillatory WSS at the center of vortex flow (cases 1-3; Figures 2 and 3). In these 5 lesions, the RRT was concentric circular from the center of vortex, and the highest RRT and OSI and lowest WSS were observed at the same point at the vortex center. On the other hand, the 2 lesions at the bleb were subjected to low WSS induced by flow expansion at the bleb (cases 4 and 5; Figure 4). In these 2 regions, the site with the maximum RRT was different from both the site with maximum OSI and the site with minimum WSS. In contrast, RRT was not markedly prolonged in aneurysms without atherosclerotic lesions.

To evaluate the risk factor of atherosclerotic change of the intracranial aneurysms, statistical analyses were performed (Table 2). Univariate analysis revealed that male sex ($P = .03$), cigarette smoking ($P = .047$), and maximum RRT ($P = .02$) are significantly related to atherosclerotic lesion on the intracranial aneurysmal wall. Of those variables that influenced atherosclerotic lesion of the intracranial aneurysmal wall, the variable male ($P = .005$) and maximum RRT ($P = .004$) remained significant in the multivariate regression model ($R^2 = 0.52$). Cigarette smoking was not chosen by the forward stepwise method. In the multivariate regression model, the variables that were not significant in the univariate analyses were eliminated.

TABLE 1. Clinical Characteristics of Patients With a Middle Cerebral Artery Aneurysm

Case	Sex, Age, y	Aneurysm Size, mm	Atherosclerotic Lesions, n	Body Mass Index, kg/m^2	Cigarette Smoking	Hypertension	Diabetes Mellitus	Dyslipidemia
1	M, 57	4.1	1	22.7	+	+	+	−
2	F, 76	7.2	2	20.9	−	−	−	+
3	M, 64	6.4	2	25.0	+	+	−	−
4	M, 53	6.1	1	27.1	+	+	−	−
5	M, 66	9.0	1	22.4	+	+	−	−
6	F, 64	6.9	0	22.7	−	+	−	+
7	F, 50	5.0	0	21.8	−	−	−	−
8	M, 32	4.6	0	30.6	−	+	−	−
9	F, 57	6.0	0	19.4	+	−	−	−
10	M, 64	5.6	0	24.2	−	+	−	−
11	M, 43	4.5	0	28.3	−	−	−	−
12	M, 63	5.9	0	21.3	+	−	−	−
13	F, 68	6.1	0	23.1	−	−	−	−
14	F, 60	7.9	0	19.2	−	−	−	−
15	F, 70	5.2	0	23.4	−	−	−	−
16	M, 64	4.7	0	27.6	+	+	+	+
17	F, 63	6.1	0	23.8	+	−	−	+
18	F, 56	4.1	0	30.9	−	+	+	+
19	F, 52	4.6	0	27.8	−	+	−	−
20	F, 62	5.3	0	32.9	−	+	−	+
21	F, 44	3.5	0	23.3	+	+	−	−
22	F, 56	4.6	0	22.9	−	−	−	−
23	M, 65	5.4	0	25.3	+	+	+	+
24	F, 65	5.1	0	19.1	−	−	−	+
25	F, 55	11.3	0	21.7	+	−	−	−
26	F, 63	6.0	0	20.4	−	+	−	−
27	F, 54	4.0	0	21.1	−	−	−	−
28	F, 74	7.9	0	22.7	−	+	−	+
29	F, 68	7.7	0	24.0	−	−	−	−
30	F, 66	6.0	0	23.4	−	+	−	+

Illustrative Cases

Case 1

A hypertensive 57-year-old man with an unruptured right MCA aneurysm of 4.1-mm maximum diameter underwent open surgery 3 months after an angiographic examination. The heterogeneous aneurysm wall with partial atherosclerosis was confirmed intraoperatively (Figure 2A). The atherosclerotic lesion of the aneurysm was subjected to disturbed blood flow indicated by prolongation of the RRT (maximum RRT = 36.1; Figure 2B). The area with prolonged RRT also had low WSS and high OSI (minimum WSS = 0.053 Pa, maximum OSI = 0.24; Figure 2B-2D). Snapshots of WSS vector plots captured at end diastole and peak systole revealed that WSS vectors were arranged in a whirl-like fashion around the vortex center, which moved around over pulsatile cycle (Figure 2E and 2F; white squares). Snapshots of the flow field (3-D streamlines) captured at end diastole and peak systole revealed an intra-aneurysmal vortex flow that moved around over pulsatile cycle and caused high OSI in the corresponding area (Figure 2G and 2H). In summary, in this case, the vortex flow induced local disturbed flow with low and oscillatory WSS, in accordance with the atherosclerotic lesion.

Case 2

A 76-year-old woman presented with subarachnoid hemorrhage. Catheter angiography revealed 4 intracranial aneurysms. Two months after the first clipping surgery of the ruptured left MCA aneurysm, an unruptured right MCA aneurysm of 7.2-mm maximum diameter was also clipped. This unruptured aneurysm had 2 yellowish atherosclerotic lesions (Figure 3A and 3B). Both atherosclerotic lesions were subjected to disturbed blood flow indicated by prolongation of the RRT (maximum RRT = 27.4 and 16.4; Figure 3C and 3D). Both areas with prolonged RRT presented high OSI (maximum OSI = 0.35 and 0.30; Figure 3E and 3F) and low WSS (minimum WSS = 0.12 and 0.15 Pa; Figure 3G and 3H). Snapshots of WSS vector plots captured at end diastole and peak systole revealed that WSS vectors were arranged in a whirl-like fashion around the vortex center (data not shown).

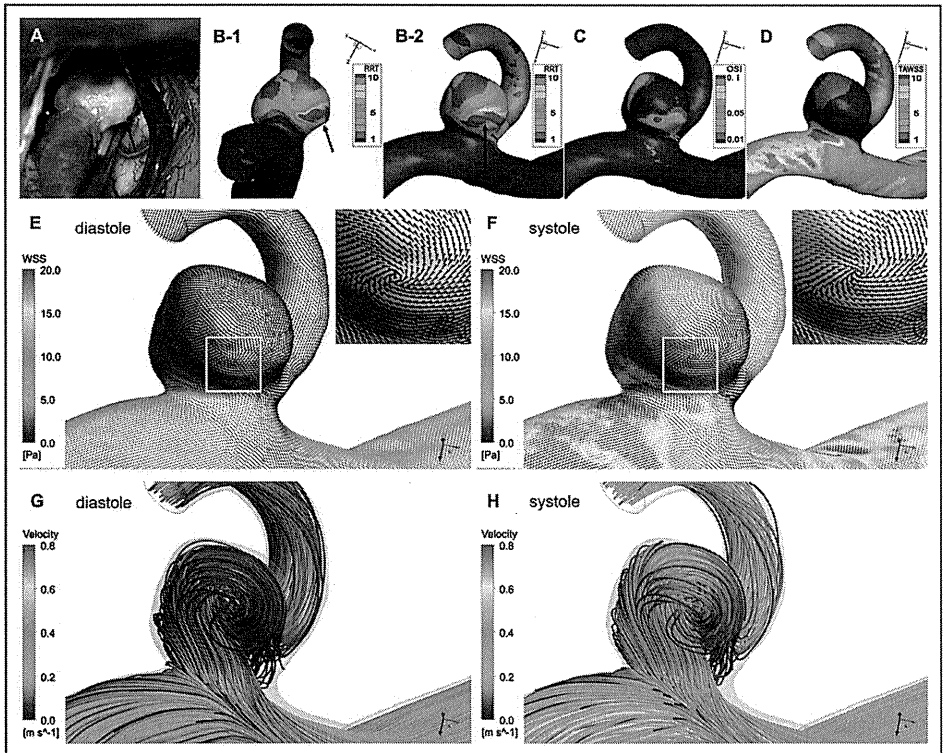

FIGURE 2. *Intraoperative photomicrograph* (**A**) *and results of computational fluid dynamics analysis* (**B-H**) *from case 1.* **A**, *intraoperative photomicrograph showing partial atherosclerosis on the aneurysm wall (arrow).* **B-1**, *contour maps of relative residence time (RRT) corresponding to the intraoperative photomicrograph showing qualitative agreement of the prolonged RRT (arrows) with the spatial distribution of atherosclerosis shown in* **A**. *RRT* (**B-2**), *oscillatory shear index (OSI;* **C**), *and time-averaged wall shear stress (WSS;* **D**) *from the same viewing angle indicate that the distribution of the area with prolonged RRT presents a high OSI value and low WSS magnitude. Snapshots of WSS vector plots captured at end diastole* (**E**) *and peak systole* (**F**) *reveal that WSS vectors are arranged in a whirl-like fashion around the vortex center* (**E** *and* **F**; *white squares). Snapshots of the flow field (3-dimensional streamlines) captured at end diastole* (**G**) *and peak systole* (**H**) *show slow and vortex flow. Maximum RRT is 36.1* (**B-1** *and* **B-2**, *arrows) and is localized at the same point as maximum OSI (0.24) and minimum WSS (0.053 Pa).*

Snapshots of the flow fields (3-D streamlines) captured at end diastole and peak systole revealed intra-aneurysmal vortices that were slow and oscillatory, in accordance with the atherosclerotic lesions of the aneurysm (data not shown).

Case 5

A 66-year-old man presented with an unruptured right MCA aneurysm of 4.0-mm maximum diameter that enlarged to a diameter of 9.0 mm 3 years after the initial MR angiography. This aneurysm had 3 blebs: 1 bleb had a yellowish atherosclerotic wall, but the other 2 blebs had reddish and rather thin walls (Figure 4A). The atherosclerotic bleb was subjected to disturbed blood flow indicated by prolongation of the RRT (Figure 4B). The area with prolonged RRT presented with low WSS but mild elevation of OSI (Figure 4B-4D). Snapshots of WSS vector plots captured at end diastole and peak systole revealed that WSS vectors were not arranged in a whirl-like fashion (Figure 4E and 4F). Snapshots of the flow field

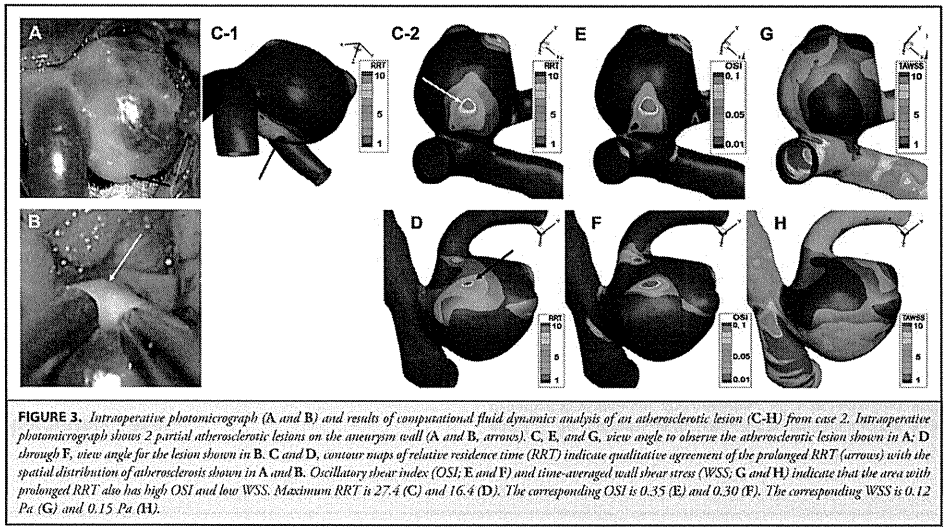

FIGURE 3. *Intraoperative photomicrograph* (**A** *and* **B**) *and results of computational fluid dynamics analysis of an atherosclerotic lesion* (**C-H**) *from case 2. Intraoperative photomicrograph shows 2 partial atherosclerotic lesions on the aneurysm wall* (**A** *and* **B**, *arrows).* **C**, **E**, *and* **G**, *view angle to observe the atherosclerotic lesion shown in* **A**; **D** *through* **F**, *view angle for the lesion shown in* **B**. **C** *and* **D**, *contour maps of relative residence time (RRT) indicate qualitative agreement of the prolonged RRT (arrows) with the spatial distribution of atherosclerosis shown in* **A** *and* **B**. *Oscillatory shear index (OSI;* **E** *and* **F**) *and time-averaged wall shear stress (WSS;* **G** *and* **H**) *indicate that the area with prolonged RRT also has high OSI and low WSS. Maximum RRT is 27.4* (**C**) *and 16.4* (**D**). *The corresponding OSI is 0.35* (**E**) *and 0.30* (**F**). *The corresponding WSS is 0.12 Pa* (**G**) *and 0.15 Pa* (**H**).

(3-D streamlines) captured at end diastole (Figure 4G) and peak systole (Figure 4H) revealed excessive slow flow, even at peak systole, that resulted from flow expansion at the bleb (Figure 4H). In summary, the atherosclerotic bleb had prolongation of RRT, accompanied not by vortex but by flow expansion at the bleb. Maximum RRT was 29.7 and the corresponding OSI and WSS were 0.03 and 0.15 Pa, respectively (Figure 4B-4D). The site with the maximum RRT was different from both the site with the maximum OSI and the site with the minimum WSS.

Case 27

A 54-year-old woman with an unruptured right MCA aneurysm of 4.0-mm maximum diameter underwent open surgery. Although this aneurysm had no atherosclerotic lesion, intraoperative video recording revealed heterogeneous wall properties: reddish translucent wall with whitish thick-walled patches (Figure 5A). The RRT was not markedly prolonged on the aneurysm. Interestingly, the area with maximum RRT (RRT = 6.6; Figure 5B), which had minimum WSS and maximum OSI (WSS = 0.28 Pa, OSI = 0.23; Figure 5C and 5D), corresponded to the whitish thick wall. It was located at the center of the tiny intra-aneurysmal vortex, which was shown by WSS vector plots and 3-D streamlines (Figure 5E-5H). In summary, in this case, a slight increase in RRT was seen at the center of the tiny intra-aneurysmal vortex, in accordance with the whitish thick wall, although the aneurysm had no atherosclerotic lesions.

DISCUSSION

To the best of our knowledge, this is the first report investigating hemodynamic characteristics of atherosclerotic lesions in intracranial aneurysms. From 30 MCA aneurysms investigated in this study, 7 atherosclerotic lesions on 5 aneurysms were identified. All 5 patients with an atherosclerotic aneurysm had several vascular atherosclerosis risk factors. Among these vascular risk factors, male sex remained an independent risk factor of the atherosclerotic aneurysmal wall lesion of the intracranial aneurysms. Although cigarette smoking did not remain significant in the multivariate analysis, it was significant in the univariate analysis and may also be important. Results of hemodynamic simulations using patient-derived inlet conditions showed that all 7 atherosclerotic lesions colocalized with the area with prolonged RRT. In contrast, aneurysms without prolonged RRT had no atherosclerotic lesions. The flow rate in each patient measured by quantitative MR velocimetry was compatible with previous data reported by Zhao et al.[18] Statistical analyses also revealed that prolongation of maximum RRT is an independent risk factor of the atherosclerotic aneurysmal wall lesion of the intracranial aneurysms.

Himburg et al[9] proposed RRT as a robust marker of disturbed blood flow with low or oscillatory WSS. From the mathematical definition of RRT, its prolongation is characterized by 2 properties: low velocity with low WSS and oscillatory behavior with high OSI. Notably, OSI is insensitive to WSS

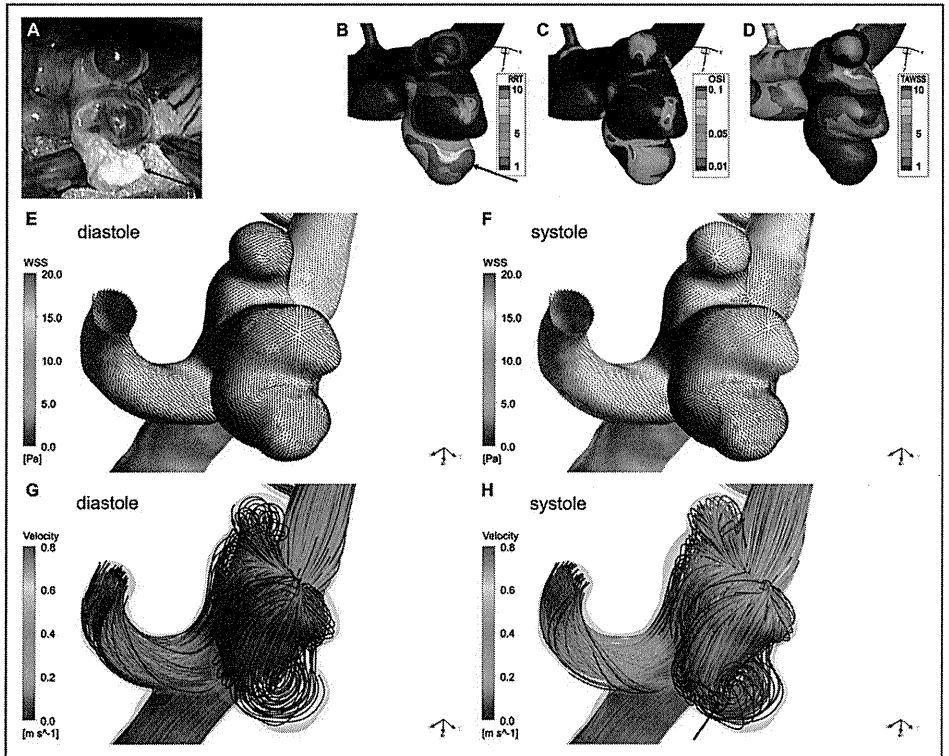

FIGURE 4. *Intraoperative photomicrograph* (**A**) *and results of computational fluid dynamics analysis of an atherosclerotic lesion* (**B**-**H**) *from case 5.* **A**, *intraoperative photomicrograph showing partial atherosclerosis on the aneurysm wall (arrow).* **B**, *a contour map of relative residence time (RRT) indicating qualitative agreement of the prolonged RRT (arrow) with the spatial distribution of atherosclerosis shown in* **A**. *RRT* (**B**), *oscillatory shear index (OSI;* **C**), *and time-averaged wall shear stress (WSS;* **D**) *from the same viewing angle indicate that the area with prolonged RRT has medium OSI and low WSS. Snapshots of WSS vector plots captured at end diastole* (**E**) *and peak systole* (**F**) *reveal that WSS vectors are not arranged in a whirl-like fashion. Snapshots of the flow field (3-dimensional streamlines) captured at end diastole* (**G**) *and peak systole* (**H**) *demonstrate extremely slow flow even at peak systole* (**H**, *arrow*). *Vortex flow is visualized near the bleb at peak systole* (**H**, *arrow*), *but RRT prolongation in this case results from the expansion of inflow to the bleb. Maximum RRT is 29.7* (**B**, *arrow*). *The corresponding OSI and WSS are 0.03 and 0.15 Pa, respectively. The site with maximum RRT is different from both the site with the maximum OSI and the site with the minimum WSS.*

magnitude, and sites with low WSS may be, but are not necessarily, sites of high OSI. Low WSS can result from flow expansion without any local flow oscillation.[9] In our study, the prolongation of RRT by an intra-aneurysmal vortex occurred with low and oscillatory WSS, whereas RRT prolongation by flow expansion at the bleb occurred with low but not oscillatory WSS. Regardless of the OSI variation, RRT could be used as a single metric for identifying atherosclerotic lesions.

This study consists of a small number of materials and lacks sequential observation with time. Therefore, results of this study can only propound a possible relation between RRT and atherogenesis on an aneurysm wall and cannot provide evidence for a causal relation. However, biomechanical links between disturbed flow and atherosclerosis are well established. Hemodynamic conditions with low and oscillatory WSS activate atherogenic and proinflammatory signaling pathways in endothelial cells[11,14] that support the focal inflammatory process that is likely to underlie atherogenesis. In addition, RRT may serve as a marker of stagnant blood flow because prolongation of the RRT means the long residence time of particles near the wall. Stagnant flow prolongs residence time of atherogenic particles in the blood, thus inducing lipid exchange and recruitment of macrophages and promoting atherosclerosis. An in vivo study revealed a correlation between oscillatory or stagnant flow and vascular atherogenesis in descending aorta; in an aortic regurgitation murine model, oscillatory and stagnant flow, indicated by elevation of OSI and RRT, accelerated atherosclerotic lesion formation.[10] These results suggest that oscillatory or stagnant blood flow, which was expressed by RRT prolongation, may be one of the necessary conditions for atherosclerotic lesion formation in intracranial aneurysms.

This study poses an important question about the role of WSS in aneurysm origin. Many hemodynamic studies of intracranial aneurysms have reported that low WSS is involved in aneurysm rupture[4,7,12] and speculated that low WSS can induce degenerative vascular wall remodeling in intracranial aneurysms, which may lead to thinning or rupture of the aneurysm wall.[13] However, the results of our study raise the possibility that an aneurysm wall exposed to low WSS can progress to atherosclerotic remodeling. Although time-dependent changes of aneurysms are unknown and the following hypothesis has no determined evidences, our hypothesis is that atherosclerotic lesion formation in intracranial aneurysms may require at least 3 conditions in addition to low WSS: Endothelial cells must exist inside the aneurysm wall, which are considered to be necessary for atherosclerotic remodeling process[19,20]; there must be an interaction between vascular endothelium and blood contents because the stagnation of blood flow might play a role in providing the long residual of atherosclerotic particles in the neighborhood of the endothelium; and the aneurysm must escape from the rupture long enough to allow atherosclerotic lesion formation. We consider that low WSS is a risk for aneurysm rupture.[12] However, aneurysms with low WSS accompanied by the stagnation of blood flow may be stabilized by atherosclerotic remodeling process if they escaped from the rupture and were exposed to stagnant blood flow for enough time. Of course, the biological response under the blood flow stagnation may be modified by the inflammatory status of the host, which is modulated by atherosclerotic risks such as smoking history and metabolic disorders.

TABLE 2. Risk Factors for Atherosclerosis on the Cerebral Aneurysmal Wall[a]

	Sex	Mean ± SD Age, y	Mean ± SD Aneurysm Size, mm	Mean ± SD Body Mass Index, kg/m²	Cigarette Smoking, n (%)	Hypertension, n (%)	Diabetes Mellitus, n (%)	Dyslipidemia, n (%)	Maximum ± SD RRT	Maximum ± SD OSI	Minimum ± SD WSS, Pa
Patients with atherosclerotic aneurysms (n = 5)	M/F: 4/1 (M: 80)	63.2 ± 8.9	6.6 ± 1.8	23.6 ± 2.4	4 (80)	4 (80)	1 (20)	1 (20)	21.7 ± 13.3	0.20 ± 0.12	0.15 ± 0.07
Patients without atherosclerotic aneurysms (n = 25)	M/F: 6/19 (M: 24)	59.1 ± 9.5	5.8 ± 1.6	24.0 ± 3.7	7 (28)	12 (48)	3 (12)	9 (36)	8.9 ± 7.9	0.26 ± 0.12	0.49 ± 0.32
P, Univariate analysis	.03	.37	.33	.81	.047	.21	.54	.89	.02	.94	.06
P, Multivariate analysis	.005								.004		

[a]OSI, oscillatory shear index; RRT, relative residence time; WSS, wall shear stress.

Limitations

In CFD simulations, typical simplifications are made in model generation and boundary condition settings.[21] Nonnewtonian viscosity was neglected for technical reasons in this study. The newtonian fluid assumption may underestimate the viscosity and overestimate WSS in regions of stasis.[22] Other limitations are related to wall compliance, outflow conditions, and the numerical technique used to solve the governing equations. These effects are

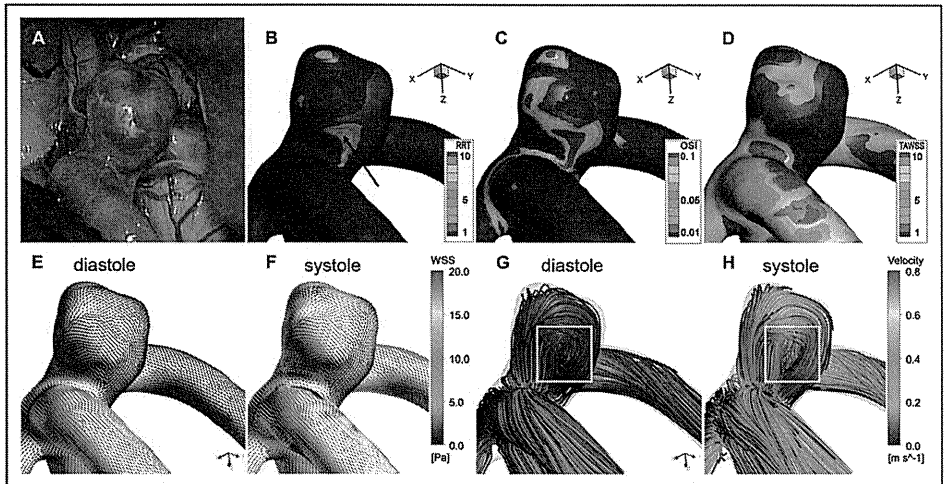

FIGURE 5. *Intraoperative photomicrograph (A) and results of computational fluid dynamics analysis (B-H) from case 27. A, intraoperative photomicrograph showing an aneurysm with some thick-walled patches but without atherosclerosis. B through D, contour maps of relative residence time (RRT; B), oscillatory shear index (OSI; C), and time-averaged wall shear stress (WSS; D) from the same viewing angle as in A. Maximum RRT is 6.6 (B, arrow) and is localized at the same point as maximum OSI (0.23) and minimum WSS (0.28 Pa). Snapshots of WSS vector plots captured at end diastole (E) and peak systole (F) showing that there is a whirl-like arrangement of WSS vectors on the surface. Snapshots of the flow field (3-dimensional streamlines) captured at end diastole (G) and peak systole (H) showing that there is a small vortex (G and H, white squares) that is localized at the point with maximum RRT and OSI.*

considered to be fairly small if the vascular geometry is correctly modeled.[16,23] Therefore, we believe that our CFD simulation using patient-derived high-resolution geometries and pulsatile inlet flow rates can reproduce the flow fields and spatial distribution of RRT. However, careful consideration should be taken in quantitative assessment of our CFD results, especially for the possibility of overestimation of WSS owing to numerical simulation under the newtonian fluid and rigid wall conditions.

CONCLUSION

The area with prolonged RRT colocalized with atherosclerotic lesions on the aneurysm wall. Intra-aneurysmal vortex and flow expansion at the bleb were recognized as local flow patterns responsible for the prolongation of RRT. Male sex and prolonged RRT were independent risk factors for atherosclerotic lesions of the intracranial aneurysms.

Disclosures

This work was supported in part by a Grant-in-Aid for Young Scientists (A) (No. 25713051; Dr Niizuma) from the Japanese Ministry of Education, Culture, Sports, Science, and Technology and a grant-in-aid from the Akaeda Medical Research Foundation (Dr Niizuma). The authors have no personal financial or institutional interest in any of the drugs, materials, or devices described in this article.

REFERENCES

1. Wiebers DO, Whisnant JP, Huston J 3rd, et al. Unruptured intracranial aneurysms: natural history, clinical outcome, and risks of surgical and endovascular treatment. *Lancet.* 2003;362(9378):103-110.
2. Morita A, Kirino T, Hashi K, et al. The natural course of unruptured cerebral aneurysms in a Japanese cohort. *N Engl J Med.* 2012;366(26):2474-2482.
3. Cebral JR, Mut F, Raschi M, et al. Aneurysm rupture following treatment with flow-diverting stents: computational hemodynamics analysis of treatment. *AJNR Am J Neuroradiol.* 2011;32(1):27-33.
4. Xiang J, Natarajan SK, Tremmel M, et al. Hemodynamic-morphologic discriminants for intracranial aneurysm rupture. *Stroke.* 2011;42(1):144-152.
5. Karmonik C, Yen C, Grossman RG, Klucznik R, Benndorf G. Intra-aneurysmal flow patterns and wall shear stresses calculated with computational flow dynamics in an anterior communicating artery aneurysm depend on knowledge of patient-specific inflow rates. *Acta Neurochir (Wien).* 2009;151(5):479-485; discussion 485.
6. Cebral JR, Mut F, Weir J, Putman CM. Association of hemodynamic characteristics and cerebral aneurysm rupture. *AJNR Am J Neuroradiol.* 2011;32(2):264-270.
7. Nixon AM, Gunel M, Sumpio BE. The critical role of hemodynamics in the development of cerebral vascular disease. *J Neurosurg.* 2010;112(6):1240-1253.
8. Qian Y, Takao H, Umezu M, Murayama Y. Risk analysis of unruptured aneurysms using computational fluid dynamics technology: preliminary results. *AJNR Am J Neuroradiol.* 2011;32(10):1948-1955.
9. Himburg HA, Grzybowski DM, Hazel AL, LaMack JA, Li XM, Friedman MH. Spatial comparison between wall shear stress measures and porcine arterial endothelial permeability. *Am J Physiol Heart Circ Physiol.* 2004;286(5):H1916-H1922.
10. Hoi Y, Zhou YQ, Zhang X, Henkelman RM, Steinman DA. Correlation between local hemodynamics and lesion distribution in a novel aortic regurgitation murine model of atherosclerosis. *Ann Biomed Eng.* 2011;39(5):1414-1422.
11. Chiu JJ, Chen CN, Lee PL, et al. Analysis of the effect of disturbed flow on monocytic adhesion to endothelial cells. *J Biomech.* 2003;36(12):1883-1895.
12. Omodaka S, Sugiyama S, Inoue T, et al. Local hemodynamics at the rupture point of cerebral aneurysms determined by computational fluid dynamics analysis. *Cerebrovasc Dis.* 2012;34(2):121-129.
13. Shojima M, Oshima M, Takagi K, et al. Magnitude and role of wall shear stress on cerebral aneurysm: computational fluid dynamic study of 20 middle cerebral artery aneurysms. *Stroke.* 2004;35(11):2500-2505.
14. Malek AM, Alper SL, Izumo S. Hemodynamic shear stress and its role in atherosclerosis. *JAMA.* 1999;282(21):2035-2042.
15. Sugiyama SI, Meng H, Funamoto K, et al. Hemodynamic analysis of growing intracranial aneurysms arising from a posterior inferior cerebellar artery. *World Neurosurg.* 2012;78(5):462-468.
16. Cebral JR, Mut F, Weir J, Putman C. Quantitative characterization of the hemodynamic environment in ruptured and unruptured brain aneurysms. *AJNR Am J Neuroradiol.* 2011;32(1):145-151.
17. He X, Ku DN. Pulsatile flow in the human left coronary artery bifurcation: average conditions. *J Biomech Eng.* 1996;118(1):74-82.
18. Zhao M, Amin-Hanjani S, Ruland S, Curcio AP, Ostergren L, Charbel FT. Regional cerebral blood flow using quantitative MR angiography. *AJNR Am J Neuroradiol.* 2007;28(8):1470-1473.
19. Kataoka K, Taneda M, Asai T, Kinoshita A, Ito M, Kuroda R. Structural fragility and inflammatory response of ruptured cerebral aneurysms: a comparative study between ruptured and unruptured cerebral aneurysms. *Stroke.* 1999;30(7):1396-1401.
20. Kataoka K, Taneda M, Asai T, Yamada Y. Difference in nature of ruptured and unruptured cerebral aneurysms. *Lancet.* 2000;355(9199):203.
21. Steinman DA, Taylor CA. Flow imaging and computing: large artery hemodynamics. *Ann Biomed Eng.* 2005;33(12):1704-1709.
22. Xiang J, Tremmel M, Kolega J, Levy EI, Natarajan SK, Meng H. Newtonian viscosity model could overestimate wall shear stress in intracranial aneurysm domes and underestimate rupture risk. *J Neurointerv Surg.* 2012;4(5):351-357.
23. Steinman DA. Image-based computational fluid dynamics modeling in realistic arterial geometries. *Ann Biomed Eng.* 2002;30(4):483-497.

***Supplemental digital content** is available for this article. Direct URL citations appear in the printed text and are provided in the HTML and PDF versions of this article on the journal's Web site (www.neurosurgery-online.com).*

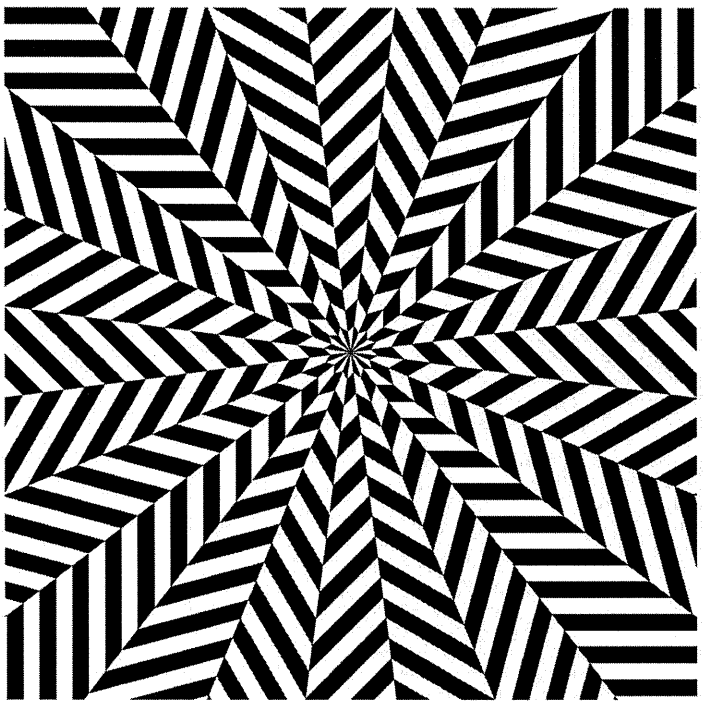

3rd International Conference on Computational and Mathematical Biomedical Engineering – CMBE2013
16-18 December 2013, Hong-Kong
P. Nithiarasu and R. Löhner (eds)

Effects of time-varying feedback signals on pressure field in ultrasonic-measurement-integrated simulation of pulsatile blood flow

Kenichi Funamoto* and Toshiyuki Hayase*
*Institute of Fluid Science, Tohoku University, 2-1-1 Katahira, Aoba-ku, Sendai 980-8577, Japan, funamoto@reynolds.ifs.tohoku.ac.jp

SUMMARY

Ultrasonic-measurement-integrated (UMI) simulation, in which feedback signals are applied to a numerical simulation based on differences between ultrasound Doppler measurement and computation, has been proposed to reproduce hemodynamics. In this study, a numerical experiment was conducted to investigate variations of the feedback signals and their effects on the pressure field in the UMI simulation of a three-dimensional pulsatile blood flow. The feedback signals and pressure in the UMI simulation showed time-dependent characteristics. Relatively large feedback signals were applied in the deceleration phase since hemodynamics became rather unstable. The adverse effect of feedback on the pressure field was reduced by the compensation method except for in the early stage of the deceleration phase.

Key Words: *hemodynamics, measurement-integrated simulation, ultrasonic measurement.*

1. INTRODUCTION

Hemodynamic wall shear stresses (WSS) and pressure are the major factors responsible for the development and progression of circulatory diseases. However, existing methodologies of measurement and computation are limited in their ability to obtain accurate and detailed information on hemodynamics. Based on the concept of flow observer [1], the authors have investigated integration of medical imaging and numerical simulation to reproduce hemodynamics and to calculate stresses acting on blood vessels [2]. An ultrasonic-measurement-integrated (UMI) simulation, in which differences between ultrasound Doppler measurement and computation are fed back to the numerical simulation, is one such method (see Fig. 1). In our former studies [2, 3], the efficiency of the UMI simulation was evaluated, and the transient and steady characteristics of the method were revealed. In addition, the effect of the feedback on the pressure field was theoretically examined, and a method of compensation for pressure field was devised [3]. However, variations of feedback signals and their effects on the pressure field in the UMI simulation of unsteady hemodynamics were unknown. In the present study, the relationships between the time-varying parameters, such as velocity error, feedback signal, and pressure, were investigated by a numerical experiment.

2. METHODS

Governing equations of the UMI simulation of blood flow are the Navier-Stokes equations and the pressure equation for incompressible and viscous fluid flow,

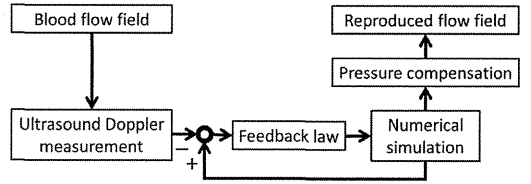

Fig. 1 Block diagram of the ultrasonic-measurement-integrated (UMI) simulation.

$$\rho\left(\frac{\partial \mathbf{u}}{\partial t}+(\mathbf{u}\cdot\nabla)\mathbf{u}\right)=\mu\Delta\mathbf{u}-\nabla p+\mathbf{f}, \tag{1}$$

$$\Delta p=-\nabla\cdot\rho(\mathbf{u}\cdot\nabla)\mathbf{u}+\nabla\cdot\mathbf{f}, \tag{2}$$

where $\mathbf{u} = (u, v, w)$ is the velocity vector, p is the pressure, t is the time, ρ is the density, and μ is the viscosity. $\mathbf{f}$ denotes the feedback signal at each feedback point and is described by the following equation.

$$\mathbf{f}=-K_v^*\frac{\Phi_d(\mathbf{u}_c-\mathbf{u}_s)}{U}\left(\frac{\rho U^2}{L}\right), \tag{3}$$

where K_v^* is the feedback gain (nondimensional), U is the characteristic velocity, L is the characteristic length, $\mathbf{u}_c$ and $\mathbf{u}_s$ are velocity vectors of the computational result and the real flow, respectively, and Φ_d (d = 1, 2, 3) is a projection function of a three-dimensional vector to the d-dimensional subspace generated by the vectors of the ultrasonic beam directions. Note that the special case with $K_v^* = 0$ is an ordinary simulation without feedback. The acquisition of Doppler velocity by projecting a velocity vector in the direction of the ultrasonic beam corresponds to the case of $d = 1$.

The application of the feedback possibly deteriorates the computational accuracy of the pressure field while improving that of the velocity field when the divergence of the feedback force vector $\mathbf{f}$ is not zero [3]. Hence, pressure deviation, p_f, caused by the application of the feedback is estimated by solving the following equation with zero value at the boundaries of the computation domain, and is subtracted from the pressure field p of the convergent result (see Fig. 1):

$$\Delta p_f=\nabla\cdot\mathbf{f}. \tag{4}$$

All parameters were nondimensionalized with the characteristic values, and the above governing equations were solved with an original program based on the SIMPLER method [2].

A numerical experiment was conducted in the same manner as in the former study [2]. Briefly, a three-dimensional configuration of a blood vessel with a thoracic aneurysm was reconstructed from CT slice images of a patient. A synthetic unsteady blood flow inside the aneurysm (Fig. 2(a)) was first defined as the standard solution with realistic unsteady velocity profiles at the upstream and downstream boundaries (see Fig. 2(b)). A UMI simulation was then carried out with simple boundary conditions: an unsteady parallel flow with a uniform velocity profile at the inlet and a free flow condition at the outlet with the same flow rate as the standard solution, considering that the exact boundary conditions of a real blood flow are usually unknown. Concerning the initial condition, a zero velocity field was applied. In the UMI simulation, the feedback signals were applied at all the grid points in the feedback domain M [0.066 m $\le z \le$ 0.106 m, dark gray zone in Fig. 2(a)], assuming the transesophageal ultrasonography of the standard solution with rotation of the probe. The ultrasound probe was assumed to be set at the same height as that of the aneurysm, the point O [(x, y, z) = (0.014 m, 0.000 m, 0.086 m)] in Fig. 2(a). Note that measurement errors such as aliasing in ultrasound Doppler measurement were not considered in this study.

The computational results were evaluated by the space-averaged error norm $\bar{e}_\Omega(a, t)$ in a monitoring domain Ω, and the time-space-averaged error norm $\bar{e}_{\Omega T}(a)$ over one cardiac cycle T

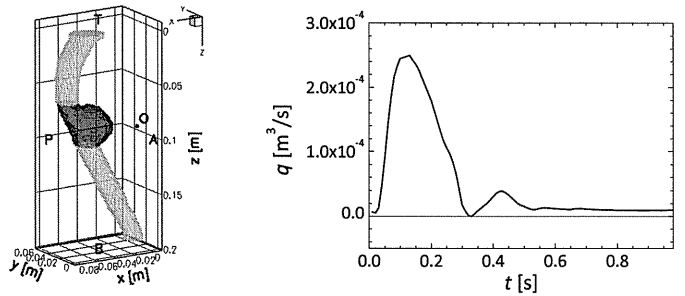

(a) (b)

Fig. 2 Computational conditions: (a) computational domain of a descending aorta with an aneurysm with feedback domain M (dark gray zone) and the origin O of the ultrasonic beam in the UMI simulation, and (b) variation of flow rate.

defined for an arbitrary variable a (velocity vector $\mathbf{u}$, Doppler velocity V, or pressure p).

3. RESULTS AND DISCUSSION

In each computation, a periodic solution was obtained within four cardiac cycles, and it was used in the following evaluation.

The inaccurate boundary conditions introduced error in velocity and pressure in the ordinary simulation without feedback ($K_v^* = 0$). In contrast, in the UMI simulation ($0 < K_v^* \leq 11$), the time-space-averaged error norm of velocity vector $\bar{e}_{M7}(\mathbf{u})$ decreased owing to the feedback. The error norm of pressure $\bar{e}_{M7}(p)$ was also reduced owing to the improvement of the computational accuracy of velocity field. However, as increasing the feedback gain in the UMI simulation without pressure compensation, the value of $\bar{e}_{M7}(p)$ gradually increased after taking a minimum value at $K_v^* = 2$. This adverse effect by the application of the feedback was properly eliminated by the pressure compensation method based on Eq. (4); the value of $\bar{e}_{M7}(p)$ became smaller and monotonically decreased as the feedback gain increased. Although the maximum feedback gain for stable computation in the UMI simulation was $K_v^* = 11$, the value of $K_v^* = 5$ was employed hereafter since the values of both $\bar{e}_{M7}(\mathbf{u})$ and $\bar{e}_{M7}(p)$ were almost constant if $K_v^* \geq 5$.

Variations of space-averaged error norms, $\bar{e}_M(V, t)$ and $\bar{e}_M(p, t)$, of Doppler velocity and pressure in the feedback domain showed periodic oscillations, as shown in Figs. 3(a) and (b). In the ordinary simulation (gray lines), the error norms are relatively small in the acceleration phase ($t \leq$ 0.13 s) though the flow rate q steeply increases (see Fig. 2(b)). This is because the blood flows as a bulk. In the deceleration phase (0.13 s $< t \leq$ 0.33 s), blood flow becomes rather unstable, and both error norms of Doppler velocity and pressure increase, showing peak values at the late stage. Then, in the diastole phase (0.33 s $< t \leq$ 0.98 s), the error norm of Doppler velocity gradually decreases, and that of pressure also decreases with some deviation. On the other hand, the UMI simulation shows smaller values of $\bar{e}_{M7}(\mathbf{u})$ and $\bar{e}_{M7}(p)$ (black lines in Figs. 3(a) and (b)) at each time phase. At the early stage of the deceleration phase (0.13 s $< t \leq$ 0.23 s), the magnitude of the feedback signal $|\mathbf{f}|$ becomes large so as to reduce the error in Doppler velocity, which increases in this period in the ordinary simulation (Figs. 3(b) and (c)). After that, the error norms of Doppler velocity and pressure, and the magnitude of the feedback signal decrease. The magnitude for pressure compensation $|p_f|$ increases due to the large feedback signals at the early stage of the deceleration phase (0.13 s $< t \leq$ 0.23 s) as shown in Fig. 3(d), but little effect of the pressure compensation is observed in Fig. 3(b). The advantageous effect of the pressure compensation is observed after the late stage of the deceleration phase (0.23 s $< t \leq$ 0.98 s). Further investigation is

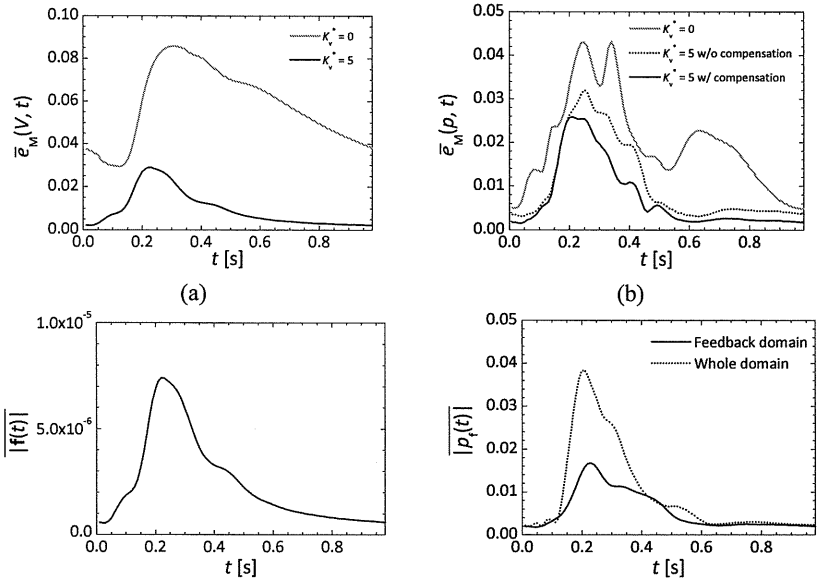

Fig. 3 Variations of space-averaged values: error norms of (a) Doppler velocity and (b) pressure in the feedback domain in the ordinary simulation ($K_v^* = 0$) and the UMI simulation with/without pressure compensation ($K_v^* = 5$), (c) magnitude of feedback signal in the feedback domain, and (d) absolute values of pressure compensation in the feedback domain and in the whole domain.

required to improve the pressure field at the early stage of the deceleration phase.

4. CONCLUSIONS

A numerical experiment revealed variations of feedback signals and their effects on the pressure field in the UMI simulation of a three-dimensional pulsatile blood flow. Relatively large feedback signals were applied in the deceleration phase since hemodynamics became rather unstable. The adverse effect of feedback on the pressure field was reduced by the compensation method except for in the early stage of the deceleration phase.

REFERENCES

[1] T. Hayase and S. Hayashi. State estimator of flow as an integrated computational method with the feedback of online experimental measurement, *Journal of Fluids Engineering,* 119, 814-822, 1997.

[2] K. Funamoto, T. Hayase, Y. Saijo, and T. Yambe. Numerical experiment for ultrasonic-measurement-integrated simulation of three-dimensional unsteady blood flow, *Annals of Biomedical Engineering,* 36, 1383-1397, 2008.

[3] K. Funamoto and T. Hayase. Reproduction of pressure field in ultrasonic-measurement-integrated simulation of blood flow, *International Journal for Numerical Methods in Biomedical Engineering,* 29, 726-740, 2013.

Novel ^{18}F-Labeled Arylquinoline Derivatives for Noninvasive Imaging of Tau Pathology in Alzheimer Disease

Nobuyuki Okamura[1], Shozo Furumoto[1,2], Ryuichi Harada[1], Tetsuro Tago[2], Takeo Yoshikawa[1], Michelle Fodero-Tavoletti[3], Rachel S. Mulligan[4], Victor L. Villemagne[4], Hiroyasu Akatsu[5], Takayuki Yamamoto[5], Hiroyuki Arai[6], Ren Iwata[2], Kazuhiko Yanai[1], and Yukitsuka Kudo[7]

[1]*Department of Pharmacology, Tohoku University School of Medicine, Sendai, Japan;* [2]*Division of Radiopharmaceutical Chemistry, Cyclotron and Radioisotope Center, Tohoku University, Sendai, Japan;* [3]*Department of Pathology, University of Melbourne, Victoria, Australia;* [4]*Department of Nuclear Medicine and Centre for PET, Austin Health, Melbourne, Victoria, Australia;* [5]*Choju Medical Institute, Fukushimura Hospital, Toyohashi, Japan;* [6]*Department of Geriatrics and Gerontology, Institute of Development, Aging and Cancer, Tohoku University, Sendai, Japan; and* [7]*Clinical Research, Innovation and Education Center, Tohoku University Hospital, Sendai, Japan*

Neurofibrillary tangles in Alzheimer disease (AD) brains are composed of the microtubule-associated protein tau. Noninvasive monitoring of tau protein aggregates in the living brain will provide useful information regarding tau pathophysiology in AD. However, no PET probes are currently available for selective detection of tau pathology in AD. We have previously reported ^{18}F-labeled THK-523 (^{18}F-6-(2-fluoroethoxy)-2-(4-aminophenyl)quinoline) as a tau imaging radiotracer candidate for PET. After compound optimization, we developed novel ^{18}F-labeled arylquinoline derivatives, ^{18}F-THK-5105 and ^{18}F-THK-5117, for use as tau imaging PET tracers. **Methods:** ^{18}F-labeled compounds were prepared from the corresponding tosylated precursors. The binding affinity of compounds to synthetic tau aggregates and tau-rich AD brain homogenates was determined by saturation and competition binding assays. The binding selectivity of compounds to tau pathology was evaluated by autoradiography of AD brain sections. The pharmacokinetics of compounds were assessed in biodistribution studies in normal mice. A 14-d toxicity study with intravenous administration of compounds was performed using rats and mice. **Results:** In vitro binding assays demonstrated higher binding affinity of THK-5105 and THK-5117 than THK-523 to tau protein aggregates and tau-rich AD brain homogenates. Autoradiographic analyses of AD brain sections showed that these radiotracers preferentially bound to neurofibrillary tangles and neuropil threads, which colocalized with Gallyas-positive and immunoreactive tau protein deposits. The distribution of this radiotracer binding in AD brain sections was completely different from that of ^{11}C-Pittsburgh compound B, showing preferential binding to amyloid plaques. Furthermore, these derivatives demonstrated abundant initial brain uptake and faster clearance in normal mice than ^{18}F-THK-523 and other reported ^{18}F-labeled radiotracers. THK-5105 and THK-5117 showed no toxic effects related to the administration of these compounds in mice and rats and no significant binding for various neuroreceptors, ion channels, and transporters at 1-μM concentrations. **Conclusion:** ^{18}F-labeled THK-5105 and THK-5117 are promising candidates as PET tau imaging radiotracers.

Key Words: Alzheimer disease; tau; neurofibrillary tangles; positron emission tomography; molecular imaging

J Nucl Med 2013; 54:1420–1427
DOI: 10.2967/jnumed.112.117341

Alzheimer disease (AD) is the most common cause of dementia in the elderly. At present, approximately 18 million people worldwide have AD, and this number is estimated to double by 2025 (*1*). The major pathologic hallmarks of AD are senile plaques (SPs) and neurofibrillary tangles (NFTs). SPs are composed of amyloid-β protein (Aβ), a 39–43 amino acid protein product derived from the proteolytic cleavage of the amyloid precursor protein. Abnormalities in the production or clearance of Aβ are considered to be the initiating events in AD pathogenesis (*2*). Excessive Aβ concentrations lead to its aggregation and formation of SPs, followed by NFT formations, synaptic dysfunction, and neuronal death. NFTs are composed of hyperphosphorylated tau, a microtubule-associated protein that stabilizes microtubule assembly in axons (*3*). Tau accumulation is also recognized as neuropil threads and dystrophic neurites in the AD brain (*4*). Phosphorylation of tau decreases its ability to bind to microtubules, which are destabilized, leading to neuronal death. NFT lesions follow a stereotypical pattern, initially appearing in the transentorhinal cortex, followed by the entorhinal cortex and the hippocampus, and subsequently the neocortex (*5*). In AD patients, the severity of tau pathology is closely related to neuronal loss (*6,7*) and cognitive impairment (*8,9*). The deposition of NFTs is thought to begin before extensive neuronal loss and cognitive decline occur. Thus, noninvasive detection of tau pathology would be useful to predict future cognitive decline in the preclinical stages of AD and to track disease progression before extensive neuronal loss occurs.

Several researchers have focused on developing radiotracers for imaging tau pathology in the human brain (*10–17*). Tau imaging radiotracers need to cross the blood–brain barrier and to have a high binding affinity to NFTs with minimal nonspecific binding (*18*). 2-(1-(6-[(2-^{18}F-fluoroethyl)(methyl)amino]-2-naphthyl)ethylidene)malononitrile (^{18}F-FDDNP) is claimed as the only PET tracer that allows measurement of the amount of tau protein deposits in the human brain (*19*). However, ^{18}F-FDDNP was found to have lower binding affinity for protein fibrils than ^{11}C-Pittsburgh compound B (^{11}C-PiB) (*20,21*). In addition, this tracer has been claimed to bind to both SPs and NFTs equally (*22*). In the neocortex of the AD brain, SPs and NFTs colocalize with each other, where Aβ concentrations are 5–20 times higher than that of tau (*23,24*). In such cases, the signal from the SPs would be so overwhelming that it would obscure the signal from the NFTs. Therefore, the development of selective tau imaging tracers is necessary for accurate and quantitative evaluation of tau pathology in AD.

In the past few years, we also have screened more than 2,000 compounds to develop novel radiotracers with high affinity and selectivity for tau aggregates. Consequently, we identified a series of novel quinoline and benzimidazole derivatives that bind NFTs and, to a lesser extent, Aβ plaques (*10*). Serial analyses of these compounds led to the design and synthesis of the novel tau imaging agent ^{18}F-6-(2-fluoroethoxy)-2-(4-aminophenyl)quinoline (^{18}F-THK-523) (*15,17*). Preclinical analyses of ^{18}F-THK-523 indicated that this tracer selectively labels tau pathology in the AD brain. However, the preclinical data suggest that the pharmacokinetics and binding characteristics of ^{18}F-THK-523 might not reach the necessary optimal levels required for PET tracers. Through our optimization process, we developed novel ^{18}F-labeled 2-arylquinoline derivatives that are promising candidates for in vivo tau imaging probes. In this study, we performed the preclinical evaluation of the binding and pharmacokinetic properties of these compounds.

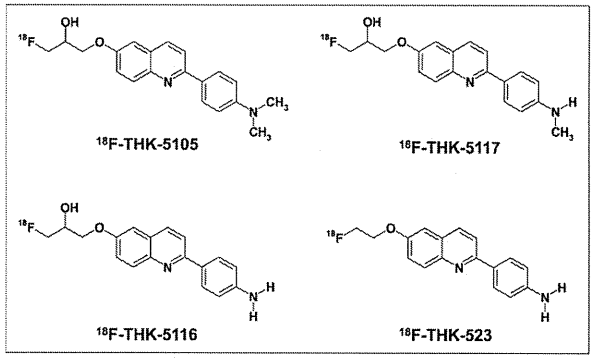

FIGURE 1. Chemical structures of ^{18}F-THK-5105, ^{18}F-THK-5116, ^{18}F-THK-5117, and ^{18}F-THK-523.

MATERIALS AND METHODS

Synthesis and Radiosynthesis of 2-Arylquinoline Derivatives

The chemical structures of 6-[(3-^{18}F-fluoro-2-hydroxy)propoxy]-2-(4-dimethylaminophenyl)quinoline (^{18}F-THK-5105), 6-[(3-^{18}F-fluoro-2-hydroxy)propoxy]-2-(4-methylaminophenyl)quinoline (^{18}F-THK-5117), 6-[(3-^{18}F-fluoro-2-hydroxy)propoxy]-2-(4-aminophenyl)quinoline (^{18}F-THK-5116), and ^{18}F-THK-523 are shown in Figure 1. ^{18}F-THK-5105, ^{18}F-THK-5116, and ^{18}F-THK-5117 were prepared from the corresponding tosylate precursors according to the scheme as indicated in the Figure 2. Details on their syntheses will be described elsewhere (S. Furumoto et al., unpublished data, 2013). Briefly, the aqueous ^{18}F$^-$ contained in the K_2CO_3 solution (1.59–3.69 GBq) and Kryptofix222 (15 mg) were placed in a brown vial. Water was removed by azeotropic evaporation with acetonitrile. After being dried, the activated ^{18}F-KF/Kryptofix222 was reacted with the precursor (3 mg) in dimethylsulfoxide (0.7 mL) at 110°C for 10 min. Then, 2 M HCl was added to the solution, followed by an additional 3-min reaction for deprotection of the hydroxyl group. After neutralization with 4 M AcOK, the product was purified by semipreparative high-performance liquid chromatography (HPLC) (column: Inertsil ODS-4 [GL Sciences, Inc.]; mobile phase: 20 mM NaH_2PO_4/acetonitrile [55/45 for THK-5105 and THK-5117, 65/35 for THK-5116]; flow rate: 5.0 mL/min). The radiolabeled product was dissolved in ethanol, dimethylsulfoxide, or saline with polysobate-80 (≤0.1%) for biologic evaluation.

^{18}F-THK-523 and ^{18}F-FDDNP were also prepared in a manner similar to the one described above using the corresponding tosylate precursors reported previously (*15,25,26*). ^{11}C-PiB was radiolabeled using its precursor (2-(4-aminophenyl)-6-methoxymethoxybenzothiazole) and ^{11}C-methyl triflate, as previously described (*27*).

Determination of Log P Values

Log P values were determined by the HPLC method according to the guideline of the Organisation for Economic Co-operation and Development (OECD Guideline for Testing of Chemicals: Partition Coefficient (n-octanol/water), High Performance Liquid Chromatography [HPLC] Method), with slight modification. Briefly, 12 reference compounds whose log P values ranged between 0.5 and 4.0 were analyzed by HPLC under the following conditions: HPLC, a JASCO LC-2000 Plus series (JASCO); column, Inertsil ODS-4 (4.6 × 150 mm, 5 μm; GL Sciences, Inc.); mobile phase, 20 mM NaH_2PO_4 (pH 7.4)/acetonitrile (55/45); flow rate, 1.5 mL/min; ultraviolet absorbance, 245 nm; and column temperature, 40°C. Then, a calibration curve of log (tR − t0) (tR, retention time; t0, dead time) versus log P of each reference compound was created (R^2 = 0.9469). Test compounds listed in Table 1 were also analyzed by the same HPLC method to measure log (tR − t0) values that were used for determination of log P values from the calibration curve.

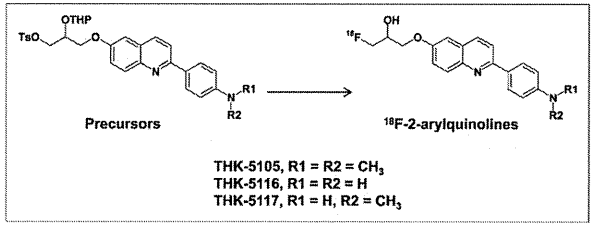

FIGURE 2. Radiosynthesis scheme of ^{18}F-2-arylquinolines.

In Vitro Binding Assays

Synthetic human Aβ1–42 was purchased from Peptide Institute Inc. Recombinant K18ΔK280-tau protein was obtained from Life Technologies Japan Ltd. Fibrils of

Received Nov. 19, 2012; revision accepted Feb. 19, 2013.
For correspondence or reprints contact: Nobuyuki Okamura, 2-1, Seiryo-machi, Aoba-ku, Sendai 980-8575 Japan.
E-mail: nookamura@med.tohoku.ac.jp
Published online Jul. 15, 2013.

TABLE 1
Log P and Brain Uptake After Intravenous Administration of ^{18}F-Labeled Compounds in Mice

Compound	Log P	Brain uptake (%ID/g) 2 min after injection	30 min after injection	60 min after injection	Brain uptake ratio (2 min/60 min)
^{18}F-THK-523	2.40	2.72	1.47	1.46	1.86
^{18}F-THK-5105	3.03	9.20	3.61	1.00	9.20
^{18}F-THK-5116	1.57	3.36	0.75	0.57	5.89
^{18}F-THK-5117	2.32	6.06	0.59	0.26	23.1
^{18}F-FDDNP	3.71	6.23	2.02	2.14	2.91

Aβ1–42 and K18ΔK280-tau were prepared as described previously (*15*). Briefly, synthetic Aβ1–42 (200 μM) and K18Δ280K-tau (20 μM) solutions in phosphate-buffered saline (PBS) were incubated at 37° C with agitation for 3–4 d. We additionally prepared AD brain homogenates for binding assay, because the structural conformation of synthetic protein fibrils does not fully correlate with the structure of native protein deposits in the human brain. Human brain tissue was isolated from a mesial temporal frozen sample of an AD patient and homogenized in PBS. Brain tissue homogenate aliquots were taken and frozen at −80°C until used. Insoluble Aβ and tau levels were determined using a human β-amyloid enzyme-linked immunosorbent assay (ELISA) kit (Wako) and a human tau ELISA kit (Life Technologies Japan Ltd.), respectively. Next, brain homogenates and the solutions of synthetic Aβ1–42 or K18Δ280K-tau fibrils were incubated with increasing concentrations of ^{18}F-THK-5105 (0.1–250 nM). To account for nonspecific binding of ^{18}F-THK-5105, the reactions were performed in triplicate in the presence of 2 μM unlabeled THK-5105. The binding reactions were incubated for 1 h at room temperature in assay buffer (Dulbecco PBS; 0.1% bovine serum albumin). Bound radioactive compounds were separated from free radioactive compounds by filtration under reduced pressure (MultiScreen HTS Vacuum Manifold; Millipore). Filters were washed three times with assay buffer, and the radioactivity contained within the filters was counted in a γ-counter (AccuFLEX γ7000, Aloka, Tokyo, Japan). Binding data were analyzed using curve-fitting software that calculates the K_d and B_{max} (K_d is dissociation constant and B_{max} is maximum number of binding sites, respectively) using nonlinear regression (GraphPad Prism; GraphPad Software).

For inhibition studies, the assay buffer containing each compound (0.1–1,000 nM), ^{18}F-THK-5105 (1.76 nM, ~37 kBq), K18Δ280K-tau (200 nM), and 0.1% bovine serum albumin was incubated at room temperature for 1 h. Nonspecific binding was determined in the presence of 10 μM THK-5105. The mixture was filtered through MultiScreen HTS 96-well filtration plates, followed by washing three times with PBS (0.1% bovine serum albumin), and the filters containing bound ^{18}F ligand were counted in a γ-counter. The percentage of bound radioligand at each concentration was measured in triplicate and then plotted against the inhibitor concentration. Half-maximal inhibitory concentration values were determined from the displacement curves using the GraphPad Prism software. Inhibition constant (K_i) values were calculated from the half-maximal inhibitory concentration values using the Cheng–Prusoff equation (*28*).

TABLE 2
K_d and B_{max} Values of ^{18}F-THK-5105 for Synthetic Tau and $Aβ_{1–42}$ Fibrils

Protein	K_{d1}	B_{max1}	K_{d2}	B_{max2}
Tau	1.45	6.89	7.40	20.05
$Aβ_{1–42}$	35.9	61.6		

K_d are in nM and Bmax are in pmol ^{18}F-THK-5105/nmol fibrils.

Tissue Staining

Experiments were performed under the regulations of the ethics committee of Tohoku University School of Medicine. Paraffin-embedded hippocampal brain sections from an autopsy-confirmed AD case (78-y-old woman) were used for tissue staining with THK-5105. Brain sections were obtained from Fukushimura Hospital. After deparaffinization, autofluorescence quenching was performed as previously described (*29*). Quenched tissue sections were immersed for 10 min in a 100-μM THK-5105 solution containing 50% ethanol. Sections were then dipped briefly into water, rinsed in PBS, coverslipped with FluorSave Reagent (Calbiochem), and examined using an Eclipse microscope (Nikon) equipped with a blue-violet filter (excitation, 400–440 nm; dichroic mirror, 455 nm; barrier filter, 470 nm). Sections stained with THK-5105 were subsequently immunostained with the AT8 anti-tau antibody (diluted 1:20; Innogenetics). After incubation at 4°C in the primary antibody for 16 h, sections were processed by the avidin-biotin method using a Pathostain ABC-POD(M) Kit (Wako) and diaminobenzidine as a chromogen. Sections were additionally stained using a modified Gallyas–Braak method (pretreatment with 0.3% potassium permanganate for 10 min, followed by 0.1% oxalic acid for 3 min) (*30*).

Autoradiography of Human Brain Sections

For the autoradiographic study, 8-μm-thick paraffin-embedded brain sections from a healthy control (62-y-old man) and 2 AD patients (69-y-old man and 92-y-old woman) were used. After deparaffinization, sections were incubated for 10 min at room temperature with radiolabeled compounds (0.5 MBq/mL) and washed briefly with water and 50% ethanol. After being dried, the labeled sections were exposed overnight to a BAS-III imaging plate (Fuji Film). The autoradiographic images were obtained using a BAS-5000 phosphoimaging instrument (Fuji Film). The neighboring sections were stained

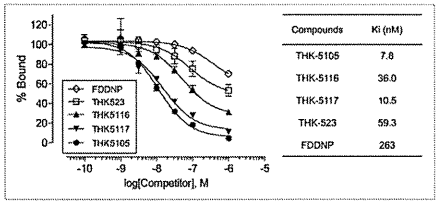

FIGURE 3. Competitive inhibition of ^{18}F-THK-5105 binding by 2-arylquinolines and FDDNP to tau protein fibrils. K_i values for inhibition of ^{18}F-THK-5105 binding to tau are shown.

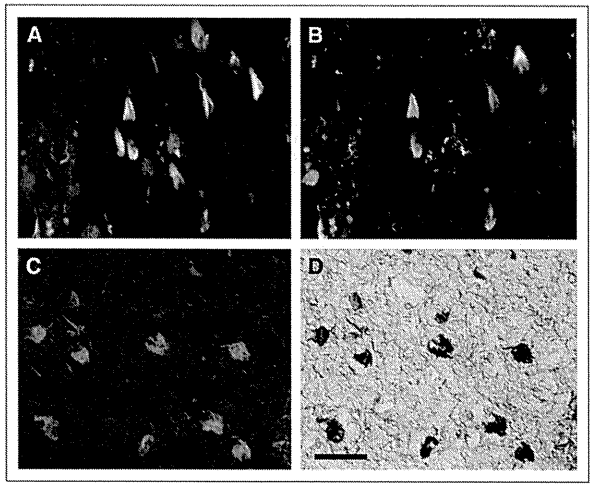

FIGURE 4. Neuropathologic staining of brain sections from AD patients. Neurofibrillary tangles and neuropil threads were clearly stained with THK-5105 (A and C). These stainings were consistent with tau immunostaining (B) and Gallyas–Braak staining (D) in same sections. Bar = 50 μm.

using a modified Gallyas–Braak method or immunostained using the AT8 anti-tau monoclonal antibody (diluted 1:20; Innogenetics), the 4G8 Aβ antibody (diluted 1:100; Signet), or the 6F/3D Aβ antibody (diluted 1:50; Dako). For correlational analysis of the autoradiographic and immunohistochemical images, 36 circular regions of interest (the area of each region of interest was ~7 mm^2) were placed on the gray matter of the hippocampus, parahippocampal gyrus, fusiform gyrus, temporal gyri (superior, middle, and inferior), insula, pre- and postcentral gyri, superior frontal gyrus, paracentral lobule, and cingulate gyrus. The percentage area of positive signals in each region of interest was calculated using ImageJ software (National Institutes of Health). A correlational analysis between percentage areas of tracer binding and positive immunostaining was performed using Pearson simple correlation.

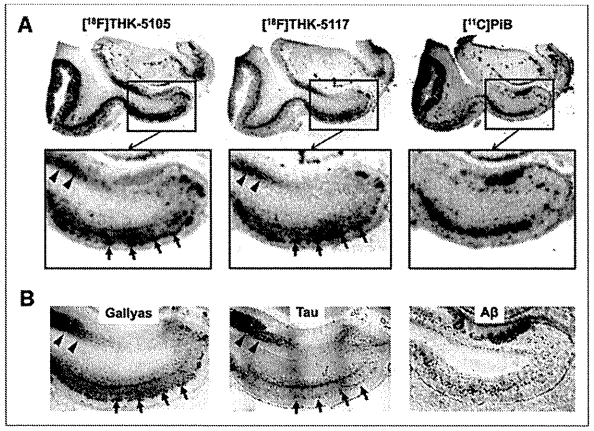

FIGURE 5. (A) Autoradiographic images of ^{18}F-THK-5105, ^{18}F-THK-5117, and ^{11}C-PiB binding in mesial temporal section from AD patient. (B) Gallyas–Braak silver staining (left) and immunostaining with anti-tau (center) and anti-Aβ (right) antibodies in adjacent brain sections. Arrowheads = CA1 area of hippocampus; longer arrows = entorhinal cortex.

Biodistribution in Mice

The experimental protocol of animal study was approved by the Ethics Committee of Tohoku University School of Medicine. ^{18}F-labeled tracers (1.1–6.3 MBq) were injected into the tail vein of male ICR mice (n = 20; mean weight, 28–32 g). Mice were then sacrificed by decapitation at 2, 10, 30, 60, and 120 min after injection. The brain, blood, liver, kidney, and femur were removed and weighed, and radioactivity was counted with an automatic γ-counter. The percentage injected dose per gram of tissue (%ID/g) was calculated by comparing tissue counts to tissue weight. Each %ID/g value is expressed as a mean ± SD of 4 separate experiments.

Animal Toxicity Studies

A 14-d toxicity study with intravenous administration of a single dose of THK-5105 and THK-5117 was performed using Sprague–Dawley rats and ICR mice. Briefly, the study included 3 groups of male and female rats and mice that were administered 0 (group 1), 0.1 (group 2), and 1 (group 3) mg/kg of test article (10% dimethylsulfoxide/90% distilled water) per rat or mouse by intravenous injection on study day 1. The study included clinical observations plus body weight measurements for a 14-d observation period. Hematology and pathologic examinations were conducted on study days 2 and 15. Detailed necropsies with external examinations were also performed.

Receptor Binding Assays

Receptor binding screens were conducted by Sekisui Medical Inc. Binding inhibition effects of 1 μM THK-5105 and THK-5117 were evaluated in competitive radioligand assays against 60 common neurotransmitter receptors, ion channels, and transporters. Percentage inhibition ratios were calculated by the following equation: inhibition ratio (%) = $[1 - (B - N)/(B_0 - N)] \times 100$, where N is the nonspecific bound radioactivity, and B and B_0 are the bound radioactivity in the presence and absence of tested compounds, respectively. Data are expressed as the mean values of duplicate samples.

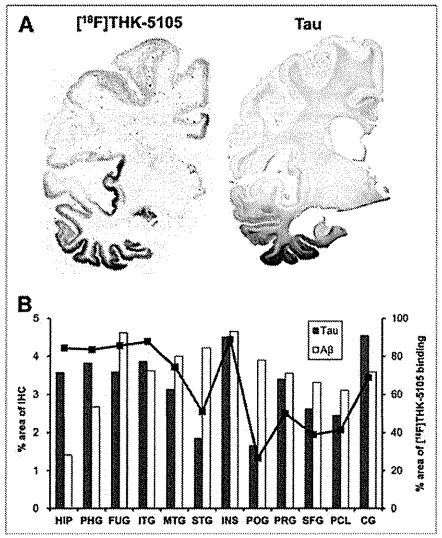

FIGURE 6. (A) Autoradiography of hemibrain sections from AD patient with ^{18}F-THK-5105 and tau immunostaining in neighboring section. (B) Region-of-interest analysis indicated that percentage areas of ^{18}F-THK-5105 binding (line plots) were significantly correlated with percentage areas of tau immunostaining (gray bars) but not with that of Aβ immunostaining (white bars). CG = cingulate gyrus; HIP = hippocampus; FUG = fusiform gyrus; IHC = immunohistochemistry; INS = insula; ITG = inferior temporal gyrus; MTG = middle temporal gyrus; PCL = paracentral lobule; PHG = parahippocampal gyrus; POG = postcentral gyrus; PRG = precentral gyrus; SFG = superior frontal gyrus; STG = superior temporal gyrus.

RESULTS

Radiosynthesis

All radiolabeled compounds were obtained in greater than 97% radiochemical purities after HPLC purification. The decay-corrected average radiochemical yields of ^{18}F-THK-523, ^{18}F-THK-5105, ^{18}F-THK-5116, ^{18}F-THK-5117, and ^{18}F-FDDNP were 58%, 48%, 41%, 48%, and 22%, respectively. The specific activities of ^{18}F-labeled compounds ranged from 37 to 110 GBq/μmol, corrected at the end of synthesis. The mean specific activity of ^{11}C-PiB was 35 GBq/μmol.

In Vitro Binding Assays

The binding properties of phenylquinoline derivatives to tau fibrils was investigated and compared with Aβ1–42 fibrils. Although only a single class of ^{18}F-THK-5105 binding sites was identified on Aβ1–42 fibrils, 2 classes of ^{18}F-THK-5105 binding sites were identified on K18Δ280-tau fibrils. As shown in Table 2, the K_d for the first class of K18Δ280-tau binding sites was 1.45 nM, indicating higher binding affinity to tau fibrils than to Aβ1–42 fibrils (K_d = 35.9 nM). Further, competitive binding assays with ^{18}F-THK-5105 displayed high binding affinity of phenylquinoline derivatives to tau fibrils (Fig. 3). The K_i for THK-5117 was 10.5 nM, indicating that THK-5117 has higher binding affinity for tau fibrils than THK-523 (K_i = 59.3 nM). In contrast, the K_i for FDDNP was 263 nM. In binding assays using mesial temporal brain homogenates containing a high density of tau (1,075 pmol/g) and moderate density of Aβ (434 pmol/g), both ^{18}F-THK-5105 (K_d = 2.63 nM; B_{max} = 358 pmol/g of tissue) and ^{18}F-THK-5117 (K_d = 5.19 nM; B_{max} = 338 pmol/g of tissue) showed higher affinity for mesial temporal brain homogenates than ^{18}F-THK-523 (K_d = 86.5 nM; B_{max} = 647.1 pmol/g of tissue) (Supplemental Fig. 1; supplemental materials are available online only at http://jnm.snmjournals.org).

Tissue Staining and Autoradiography

The selective binding ability of the compounds was further examined using AD brain sections. The fluorescent compound THK-5105 clearly stained NFTs and neuropil threads in the hippocampal section of an AD patient (Fig. 4A). Selective binding of this compound with tau pathology was confirmed by comparing with the results of tau immunohistochemistry for the same sections (Fig. 4B). In contrast, SPs were faintly stained with THK-5105. Further, we compared findings of THK-5105 staining with those of Gallyas–Braak silver staining, a conventional technique used to visualize tau pathology in the AD brain (Figs. 4C and 4D), and the binding of THK-5105 to NFTs and neuropil threads was confirmed. The images of staining with THK-5116 and THK-5117 were similar to those with THK-5105 (data not shown).

To investigate the binding ability of ^{18}F-THK-5105 and ^{18}F-THK-5117 to NFTs at tracer doses, in vitro autoradiography was performed in postmortem AD brain sections, and the findings were compared with Gallyas–Braak staining and immunohistochemistry. In the mesial temporal sections, laminar distributions of ^{18}F-THK-5105 and ^{18}F-THK-5117 were observed in the deep layer of gray matter (Fig. 5A). A high density of tracer accumulation was observed in the CA1 area of the hippocampus, which is reported as the most frequent site for NFTs in AD (*31*). These tracer distributions coincided with Gallyas–Braak staining and tau immunostaining (Fig. 5B) but not with the distribution of ^{11}C-PiB (Fig. 5A) and Aβ immunostaining (Fig. 5B). In contrast, no significant accumulation of ^{18}F-THK-5105 and ^{18}F-THK-5117 was observed in the hippocampus of the healthy control subject (Supplemental Fig. 2). ^{18}F-THK-5116 failed to give a specific signal in the AD brain sections (data not shown).

To further assess the regional differences of tracer binding in the AD brain, ^{18}F-THK-5105 autoradiography was conducted using AD hemibrain sections and compared with the Aβ PET tracer ^{11}C-PiB (*32*). ^{18}F-THK-5105 densely accumulated in the gray matter of the hippocampus, parahippocampal gyrus, fusiform gyrus, inferior and middle temporal gyri, insula, and cingulate gyrus (Fig. 6A), regions known for the abundance of tau pathology in AD (*33*). In contrast, tracer binding in the parietal areas was modest. The pattern of tracer distribution correlated with the known distribution of tau pathology (Fig. 6A) but not with the known distribution of Aβ or the binding of ^{11}C-PiB (data not shown). In addition, quantitative analyses of these images demonstrated a significant correlation of ^{18}F-THK-5105 binding with tau immunostained areas but not with the areas of Aβ immunostaining (Fig. 6B; Supplemental Fig. 3). In contrast, ^{11}C-PiB bindings showed a good correlation with Aβ deposition but not with tau deposition (Supplemental Fig. 3).

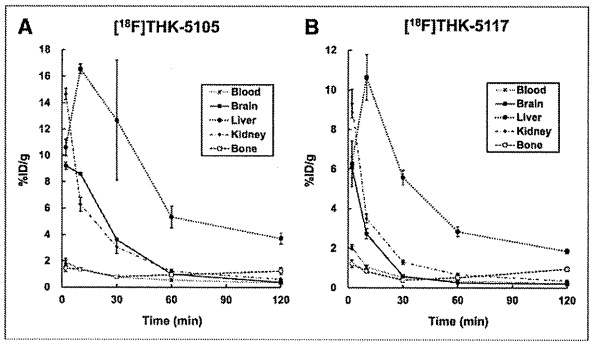

FIGURE 7. Time–activity curves after intravenous administration of ^{18}F-THK-5105 (A) and ^{18}F-THK-5117 (B) in mice.

Pharmacokinetics in Mice

All tested compounds exhibited sufficient amounts of tracer uptake in the mouse brain immediately after intravenous administration. Compared with ^{18}F-THK-523, new compounds showed significantly higher brain uptake at 2 min after injection (Table 1). ^{18}F-THK-5105 showed the highest brain uptake. In addition, clearance of these derivatives from normal brain tissue was faster than that of ^{18}F-THK-523 and ^{18}F-FDDNP (Table 1). The brain uptake ratio at 2 versus 60 min was highest for ^{18}F-THK-5117, followed by ^{18}F-THK-5105, ^{18}F-THK-5116, ^{18}F-FDDNP, and ^{18}F-THK-523. After injection of ^{18}F-THK-5105 and ^{18}F-THK-5117, the regional tracer uptake in the liver was highest at 10 min after injection, and the tracer was then slowly washed out from the body (Fig. 7). Compared with ^{18}F-THK-5105, ^{18}F-THK-5117 tended to have faster clearance from the brain, blood, liver, and kidney. No remarkable accumulation of ^{18}F-THK-5105 and ^{18}F-THK-5117 was observed in the bone.

Animal Toxicity Studies

A single intravenous administration of THK-5105 and THK-5117 at 1 mg/kg, equivalent to 100,000-fold the intended clinical dose for humans, caused no systemic toxicity in rats or mice. There were no unscheduled deaths or morbidity detected in this study. During the experimental period, the body weight of all animals increased normally, and no treatment-related changes were noted in any animals. There were no major clinical, biochemical, or histopathologic findings associated with the administration of THK-5105 and THK-5117.

Receptor Binding Assays

Binding inhibition of THK-5105 and THK-5117 was assessed in competitive radioligand binding assays against 60 common neurotransmitter receptors, ion channels, and transporters. As a result, no remarkable inhibition (<50%) was observed for various receptors, ion channels, and transporters at 1-μM concentrations of THK-5105 and THK-5117.

DISCUSSION

These findings suggest that ^{18}F-THK-5105 and ^{18}F-THK-5117 are promising candidates as tau imaging PET probes. Although previous saturation analysis showed the high binding affinity of ^{18}F-THK-523 for tau fibrils (K_d = 1.67 nM), the current competition assay demonstrated relatively lower binding affinity of THK-523 for tau fibrils (K_i = 59.3 nM) than THK-5105 (K_i = 7.8 nM) and THK-5117 (K_i = 10.5 nM). ^{18}F-THK-5105 showed higher affinity for tau pathology than for Aβ pathology in AD brain sections. Most amyloid imaging agents potentially bind to both tau and Aβ fibrils, because both protein fibrils share a common β-sheet secondary structure. To ensure the binding specificity of these compounds as tau-selective PET probes, the binding affinity to Aβ fibrils should be below the in vivo detection threshold. In vitro binding assays indicated that the binding affinity of ^{18}F-THK-5105 for Aβ fibrils (K_d = 35.9 nM) was 25 times lower than for tau fibrils (K_d = 1.45 nM). This K_d would allow selective detection of tau pathology, because the usual required K_d values for imaging Aβ are below 20 nM (*34*). However, the required K_d value for imaging tau deposits is still unknown. Considering that the concentrations of tau are about an order of magnitude lower than those of Aβ, the K_d value for tau should be well below 20 nM, in the low nanomolar range, to allow sensitive detection of tau pathology. In that respect, the binding affinities of both ^{18}F-THK-5105 and ^{18}F-THK-5117 to tau fibrils may be sufficient for in vivo detection of tau pathology in the brain. However, in vitro binding assay data should be carefully interpreted, because the structural conformation of synthetic tau fibrils does not fully correlate with the structure of NFTs and neuropil threads in the human brain. Actually, ^{18}F-THK-523 showed substantially lower affinity for AD brain homogenates (Kd = 86.5 nM) than for synthetic tau protein fibrils (Kd = 1.67 nM) (*15*). In the future, in vitro binding data should be compared with in vivo PET data to determine the required K_d value for in vivo tau detection.

In vitro assays using human brain samples are considered more reliable for evaluating the binding selectivity of radiotracers to tau and Aβ pathology at tracer doses. Autoradiography studies using human brain sections demonstrated the preferential binding of ^{18}F-THK-5105 and ^{18}F-THK-5117 to tau protein deposits in the AD brain. We observed a high density of ^{18}F-THK-5105 and ^{18}F-THK-5117 binding in the CA1 region of AD hippocampus, which contained substantial amounts of NFTs and neuropil threads. In addition, these tracers clearly visualized the laminar distribution of tau in the pri-α layer of the transentorhinal and temporal cortices, which is typically observed in the AD brain (*5*). The distribution pattern of THK tracer binding in AD brains was different from that of the Aβ imaging probe PiB and BF-227, which showed diffuse punctate distribution in broad neocortical gray matter and less tracer distribution in the mesial temporal region. These findings strongly suggest that binding properties of ^{18}F-THK-5105 and ^{18}F-THK-5117 are different from those of currently available Aβ PET probes. Compared with ^{18}F-THK-523 (*17*), both ^{18}F-THK-5105 and ^{18}F-THK-5117 showed higher contrast of tau pathology in autoradiographic images. These findings most likely reflect the increased binding affinity to tau by methylation of the amino group, as indicated by in vitro binding assays.

Similar findings were previously reported in an arylbenzothiazole derivative (*35*). Compared with ^{18}F-THK-5105, ^{18}F-THK-5117 showed lesser tracer binding in the gray matter containing high density of Aβ plaques, suggesting low binding affinity to Aβ and high selectivity to tau. ^{18}F-THK-5105 tends to show higher signals in the gray matter, and some of the images of ^{18}F-THK-5105 binding showed the patchy pattern as observed for ^{11}C-PiB binding. One possible reason for this is the binding of ^{18}F-THK-5105 to tau protein in dystrophic neurites. Another possible reason is binding of ^{18}F-THK-5105 to Aβ fibrils. However, the latter explanation seems unlikely given that ^{18}F-THK-5105 binding, as clearly shown in Figure 6, was correlated with tau, and not Aβ, deposits.

In vitro binding assays using AD brain homogenates are generally used to measure the binding affinity of Aβ imaging radiotracers to SPs or NFTs and the number of binding sites in real AD pathology (*36*). For most of the useful Aβ imaging radiotracers, the reported K_d or K_i values for neocortical brain samples are below 10 nM (*36,37*). In this study, the K_d values for high-affinity sites of AD mesial temporal homogenates were 2.63 nM for ^{18}F-THK-5105 and 5.19 nM for ^{18}F-THK-5117. These binding affinities were higher than that for ^{18}F-THK-523 and appear to be sufficient for the in vivo detection of AD pathology in the mesial temporal region at tracer doses. Furthermore, the B_{max}/K_d ratios of ^{18}F-THK-5105 and ^{18}F-THK-5117 for AD brain homogenates were 136.1 and 65.1, respectively, which fulfills the criteria (B_{max}/K_d ratio > 10) for a good neuroimaging agent (*35*).

The optimization of pharmacokinetics is an important aspect in the development of a PET tracer (*38*). ^{18}F-THK-5105, ^{18}F-THK-5116, and ^{18}F-THK-5117 fulfilled the criteria of appropriate log P value (log P = 1–3) for brain entry (*39*). In mice, these tracers showed sufficient brain uptake and rapid washout from normal brain tissue. ^{18}F-THK-5105 and ^{18}F-THK-5117 exhibited high initial brain uptake in normal mice (>6 %ID/g at 2 min). These values, which are equivalent to over 100% injected dose index in a 25-g mouse, meet the prerequisites for useful PET imaging agents (*34*). The 2- to 60-min ratio of radioactivity concentrations for ^{18}F-THK-5117 was 23.1, indicating faster washout from normal brain for these compounds than for other currently available ^{18}F-labeled tracers such as ^{18}F-FDDNP (2.91), ^{18}F-florbetaben (4.83) (*40*), and ^{18}F-florbetapir (3.90) (*37*). Compared with ^{18}F-THK-523, ^{18}F-THK-5116 washed out faster from normal brain tissue of mice, indicating that the hydroxylation of the fluoroalkoxy group improves pharmacokinetics in mice. However ^{18}F-THK-5116 is not a suitable compound for clinical application, because of its lower initial brain uptake and binding affinity than the other 2 compounds.

CONCLUSION

^{18}F-THK-5105 and ^{18}F-THK-5117 should be considered as promising candidates for PET tau imaging radiotracers. Future clinical studies will clarify the usefulness of these radiotracers for the early detection of AD tau pathology.

DISCLOSURE

The costs of publication of this article were defrayed in part by the payment of page charges. Therefore, and solely to indicate this fact, this article is hereby marked "advertisement" in accordance with 18 USC section 1734. This study was supported by the research fund from GE Healthcare; the Industrial Technology Research Grant Program of the NEDO in Japan (09E51025a); Health and Labor Sciences Research grants from the Ministry of Health, Labor, and Welfare of Japan; and a Grant-in-Aid for Scientific Research (B) (23390297) and "Japan Advanced Molecular Imaging Program (J-AMP)" of the Ministry of Education, Culture, Sports, Science and Technology (MEXT), Japan. No other potential conflict of interest relevant to this article was reported.

REFERENCES

1. Organisation for Economic Co-operation and Development (OECD). *Understanding the Brain: The Birth of a Learning Science*. Paris, France: OECD Publishing; 2007.
2. Hardy J, Selkoe DJ. The amyloid hypothesis of Alzheimer's disease: progress and problems on the road to therapeutics. *Science*. 2002;297:353–356.
3. Lichtenberg B, Mandelkow EM, Hagestedt T, Mandelkow E. Structure and elasticity of microtubule-associated protein tau. *Nature*. 1988;334:359–362.
4. Holzer M, Holzapfel HP, Zedlick D, Bruckner MK, Arendt T. Abnormally phosphorylated tau protein in Alzheimer's disease: heterogeneity of individual regional distribution and relationship to clinical severity. *Neuroscience*. 1994;63:499–516.
5. Braak H, Braak E. Neuropathological stageing of Alzheimer-related changes. *Acta Neuropathol*. 1991;82:239–259.
6. Bondareff W, Mountjoy CQ, Roth M, Hauser DL. Neurofibrillary degeneration and neuronal loss in Alzheimer's disease. *Neurobiol Aging*. 1989;10:709–715.
7. Bobinski M, Wegiel J, Wisniewski HM, et al. Neurofibrillary pathology: correlation with hippocampal formation atrophy in Alzheimer disease. *Neurobiol Aging*. 1996;17:909–919.
8. Guillozet AL, Weintraub S, Mash DC, Mesulam MM. Neurofibrillary tangles, amyloid, and memory in aging and mild cognitive impairment. *Arch Neurol*. 2003;60:729–736.
9. Gómez-Isla T, Price JL, McKeel DW Jr., Morris JC, Growdon JH, Hyman BT. Profound loss of layer II entorhinal cortex neurons occurs in very mild Alzheimer's disease. *J Neurosci*. 1996;16:4491–4500.
10. Okamura N, Suemoto T, Furumoto S, et al. Quinoline and benzimidazole derivatives: candidate probes for in vivo imaging of tau pathology in Alzheimer's disease. *J Neurosci*. 2005;25:10857–10862.
11. Rojo LE, Alzate-Morales J, Saavedra IN, Davies P, Maccioni RB. Selective interaction of lansoprazole and astemizole with tau polymers: potential new clinical use in diagnosis of Alzheimer's disease. *J Alzheimers Dis*. 2010;19:573–589.
12. Ono M, Hayashi S, Matsumura K, et al. Rhodanine and thiohydantoin derivatives for detecting tau pathology in Alzheimer's brains. *ACS Chem Neurosci*. 2011;2:269–275.
13. Jensen JR, Cisek K, Funk KE, Naphade S, Schafer KN, Kuret J. Research towards tau imaging. *J Alzheimers Dis*. 2011;26(suppl 3):147–157.
14. Zhang W, Arteaga J, Cashion DK, et al. A highly selective and specific PET tracer for imaging of tau pathologies. *J Alzheimers Dis*. 2012;31:601–612.
15. Fodero-Tavoletti MT, Okamura N, Furumoto S, et al. ^{18}F-THK523: a novel in vivo tau imaging ligand for Alzheimer's disease. *Brain*. 2011;134:1089–1100.
16. Villemagne VL, Furumoto S, Fodero-Tavoletti MT, et al. The challenges of tau imaging. *Future Neurol*. 2012;7:409–421.
17. Harada R, Okamura N, Furumoto S, et al. Comparison of the binding characteristics of [^{18}F]THK-523 and other amyloid imaging tracers to Alzheimer's disease pathology. *Eur J Nucl Med Mol Imaging*. 2013;40:125–132.
18. Small GW, Agdeppa ED, Kepe V, Satyamurthy N, Huang SC, Barrio JR. In vivo brain imaging of tangle burden in humans. *J Mol Neurosci*. 2002;19:323–327.
19. Agdeppa ED, Kepe V, Liu J, et al. Binding characteristics of radiofluorinated 6-dialkylamino-2-naphthylethylidene derivatives as positron emission tomography imaging probes for beta-amyloid plaques in Alzheimer's disease. *J Neurosci*. 2001;21:RC189.
20. Thompson PW, Ye L, Morgenstern JL, et al. Interaction of the amyloid imaging tracer FDDNP with hallmark Alzheimer's disease pathologies. *J Neurochem*. 2009;109:623–630.
21. Tolboom N, Yaqub M, van der Flier WM, et al. Detection of Alzheimer pathology in vivo using both ^{11}C-PIB and ^{18}F-FDDNP PET. *J Nucl Med*. 2009;50:191–197.
22. Shoghi-Jadid K, Small GW, Agdeppa ED, et al. Localization of neurofibrillary tangles and beta-amyloid plaques in the brains of living patients with Alzheimer disease. *Am J Geriatr Psychiatry*. 2002;10:24–35.
23. Näslund J, Haroutunian V, Mohs R, et al. Correlation between elevated levels of amyloid beta-peptide in the brain and cognitive decline. *JAMA*. 2000;283:1571–1577.
24. Mukaetova-Ladinska EB, Harrington CR, Roth M, Wischik CM. Biochemical and anatomical redistribution of tau protein in Alzheimer's disease. *Am J Pathol*. 1993;143:565–578.
25. Liu J, Kepe V, Zabjek A, et al. High-yield, automated radiosynthesis of 2-(1-{6-[(2-[^{18}F]fluoroethyl)(methyl)amino]-2-naphthyl}ethylidene)malononitrile ([^{18}F] FDDNP) ready for animal or human administration. *Mol Imaging Biol*. 2007;9:6–16.
26. Fodero-Tavoletti MT, Mulligan RS, Okamura N, et al. In vitro characterisation of BF227 binding to alpha-synuclein/Lewy bodies. *Eur J Pharmacol*. 2009;617:54–58.
27. Wilson AA, Garcia A, Chestakova A, Kung H, Houle S. A rapid one-step radiosynthesis of the beta-amyloid imaging radiotracer N-methyl-[C-11]2-(4'-methylaminophenyl)-6-hydroxybenzothiazole ([C-11]-6-OH-BTA-1). *J Labelled Comp Radiopharm*. 2004;47:679–682.
28. Cheng Y, Prusoff WH. Relationship between the inhibition constant (Ki) and the concentration of inhibitor which causes 50 per cent inhibition (IC50) of an enzymatic reaction. *Biochem Pharmacol*. 1973;22:3099–3108.
29. Okamura N, Suemoto T, Shimadzu H, et al. Styrylbenzoxazole derivatives for in vivo imaging of amyloid plaques in the brain. *J Neurosci*. 2004;24:2535–2541.
30. Ikeda K, Akiyama H, Kondo H, Haga C. A study of dementia with argyrophilic grains. Possible cytoskeletal abnormality in dendrospinal portion of neurons and oligodendroglia. *Acta Neuropathol*. 1995;89:409–414.
31. Bouras C, Hof PR, Giannakopoulos P, Michel JP, Morrison JH. Regional distribution of neurofibrillary tangles and senile plaques in the cerebral cortex of elderly patients: a quantitative evaluation of a one-year autopsy population from a geriatric hospital. *Cereb Cortex*. 1994;4:138–150.
32. Kudo Y, Okamura N, Furumoto S, et al. 2-(2-[2-Dimethylaminothiazol-5-yl] ethenyl)-6- (2-[fluoro]ethoxy)benzoxazole: a novel PET agent for in vivo detection of dense amyloid plaques in Alzheimer's disease patients. *J Nucl Med*. 2007;48:553–561.
33. Braak H, Alafuzoff I, Arzberger T, Kretzschmar H, Del Tredici K. Staging of Alzheimer disease-associated neurofibrillary pathology using paraffin sections and immunocytochemistry. *Acta Neuropathol*. 2006;112:389–404.
34. Mathis CA, Wang Y, Klunk WE. Imaging beta-amyloid plaques and neurofibrillary tangles in the aging human brain. *Curr Pharm Des*. 2004;10:1469–1492.
35. Mathis CA, Wang Y, Holt DP, Huang GF, Debnath ML, Klunk WE. Synthesis and evaluation of ^{11}C-labeled 6-substituted 2-arylbenzothiazoles as amyloid imaging agents. *J Med Chem*. 2003;46:2740–2754.
36. Klunk WE, Wang Y, Huang GF, et al. The binding of 2-(4'-methylaminophenyl) benzothiazole to postmortem brain homogenates is dominated by the amyloid component. *J Neurosci*. 2003;23:2086–2092.
37. Choi SR, Golding G, Zhuang Z, et al. Preclinical properties of ^{18}F-AV-45: a PET agent for Abeta plaques in the brain. *J Nucl Med*. 2009;50:1887–1894.
38. Furumoto S, Okamura N, Iwata R, Yanai K, Arai H, Kudo Y. Recent advances in the development of amyloid imaging agents. *Curr Top Med Chem*. 2007;7:1773–1789.
39. Waterhouse RN. Determination of lipophilicity and its use as a predictor of blood-brain barrier penetration of molecular imaging agents. *Mol Imaging Biol*. 2003;5:376–389.
40. Zhang W, Oya S, Kung MP, Hou C, Maier DL, Kung HF. F-18 Polyethyleneglycol stilbenes as PET imaging agents targeting Abeta aggregates in the brain. *Nucl Med Biol*. 2005;32:799–809.

J Gastroenterol (2014) 49:231–238
DOI 10.1007/s00535-013-0797-y

The Japanese Society of Gastroenterology

ORIGINAL ARTICLE—ALIMENTARY TRACT

Long-term incidence and characteristics of intestinal failure in Crohn's disease: a multicenter study

Kazuhiro Watanabe · Iwao Sasaki · Kouhei Fukushima · Kitaro Futami · Hiroki Ikeuchi · Akira Sugita · Riichiro Nezu · Tsunekazu Mizushima · Shingo Kameoka · Masato Kusunoki · Kazuhiko Yoshioka · Yuji Funayama · Toshiaki Watanabe · Hisao Fujii · Mamoru Watanabe

Received: 28 December 2012 / Accepted: 14 March 2013 / Published online: 7 April 2013

Abstract
Background The aim of this study was to clarify the risk and characteristics of intestinal failure (IF) in patients with Crohn's disease (CD).
Methods The present study was a retrospective study in 12 hospitals. CD patients who underwent initial surgery at any of the 12 hospitals between 1970 and 2009 were collected ($n = 1{,}703$). Those who developed IF were reviewed ($n = 68$), and the cumulative risk of IF was analyzed by the Kaplan–Meier method. In addition, IF patients who underwent initial surgery at other hospitals and were then treated at any of the 12 hospitals were also reviewed ($n = 33$). Thus, a total of 101 IF patients were collected, and the cumulative risk of IF-related death was analyzed.
Results The cumulative risk of IF after the initial surgery was 0.8 % (5 years), 3.6 % (10 years), 6.1 % (15 years), and 8.5 % (20 years). In CD patients with IF, mean age at initial surgery, IF occurrence, and present age at the time of the study were 28.2, 38.2, and 46.1 years, respectively. The mean number of surgeries per patient was 3.3. The mean length of the remnant small bowel was 163 cm. Twelve IF patients (12 %) had died and the cumulative risk of IF-related death by the time from the occurrence of IF was 1.1 % (3 years), 3.7 % (5 years), 6.5 % (7 years), and 8.9 % (10 years).
Conclusion The occurrence of IF and IF-related death in CD patients is not rare over the long term. There is a pressing need to develop strategies for the prevention and management of IF.

Keywords Crohn's disease · Intestinal failure · Short bowel syndrome · Home parenteral nutrition · Surgery

The present study was performed as a project study under the Surgical Research Group, the Research Committee of Inflammatory Bowel Disease, Ministry of Health, Labour and Welfare of Japan.

A portion of the data from the present study was presented as a symposium session at the 112th Annual Congress of Japan Surgical Society, April 12–14, 2012, Makuhari, Japan.

K. Watanabe (✉) · I. Sasaki · K. Fukushima
Department of Surgery, Tohoku University Hospital, 1-1 Seiryo-machi, Aoba-ku, Sendai, Miyagi, Japan
e-mail: k-wata@surg1.med.tohoku.ac.jp

K. Fukushima
Laboratory of GI Tract Reconstruction, Tohoku University Graduate School of Biomedical Engineering, Sendai, Japan

K. Fukushima
Department of Molecular and Surgical Pathophysiology, Tohoku University Graduate School of Medicine, Sendai, Japan

K. Futami
Department of Surgery, Fukuoka University Chikushi Hospital, Fukuoka, Japan

H. Ikeuchi
Inflammatory Bowel Disease Center, Hyogo College of Medicine, Nishinomiya, Japan

A. Sugita
Department of Surgery, Yokohama Municipal Citizen's Hospital, Yokohama, Japan

R. Nezu
Department of Surgery, Osaka Rosai Hospital, Sakai, Japan

T. Mizushima
Department of Gastroenterological Surgery, Osaka University Hospital, Suita, Japan

S. Kameoka
Department of Surgery II, Tokyo Women's Medical University, Tokyo, Japan

M. Kusunoki
Department of Gastrointestinal and Pediatric Surgery, Mie University Hospital, Tsu, Japan

Introduction

Crohn's disease (CD) is a chronic inflammatory gastrointestinal disorder with a high recurrence rate. It is estimated that up to 80 % of patients with CD will require at least one intestinal surgery during their course [1–4]. The rates of recurrence requiring re-operation from the first surgery are reported to range from 16 to 36 % at 5 years and from 28 to 55 % at 10 years [3–6]. Although medical and surgical management aims to prevent recurrence and minimize the extent of resection [7], CD patients often require multiple surgeries, which increases the risk for intestinal failure (IF).

The term IF was originally defined by Fleming and Remington as a reduction in functioning gut mass below the minimum necessary for adequate digestion and absorption of nutrients [8]. Initially, this definition was often used to describe patients who require home parenteral nutrition (HPN) to survive, without taking into account the patients who simply require fluid [9]. Recently, the definition has been broadened, and an international consensus group proposed that IF be characterized by the inability to maintain protein-energy, fluid, electrolyte, or micronutrient balance, which results from obstruction, dysmotility, surgical resection, congenital defect, or disease-associated loss of absorption [10].

K. Yoshioka
Department of Surgery, Kansai Medical University Kouri Hospital, Osaka, Japan

Y. Funayama
Department of Colorectal Surgery, Tohoku Rosai Hospital, Sendai, Japan

T. Watanabe
Department of Surgical Oncology, The University of Tokyo, Tokyo, Japan

H. Fujii
Department of Endoscopy, Nara Medical University Hospital, Kashihara, Japan

M. Watanabe
Department of Gastroenterology, Tokyo Medical and Dental University, Tokyo, Japan

Among patients with CD who receive long-term treatment, IF is one of the most serious complications. However, there have been few reports concerning the occurrence rate and characteristics of IF in CD patients. The aim of the present study was to clarify the risk and characteristics of IF in CD patients after intestinal surgery.

Methods

Participating hospitals

This retrospective study was performed at the following 12 Japanese hospitals, which were participants in the study group of inflammatory bowel disease, sponsored by the Japanese Ministry of Health, Labour and Welfare: Tohoku University Hospital, Fukuoka University Chikushi Hospital, Hyogo Medical University Hospital, Yokohama Municipal Citizen's Hospital, Osaka Rosai Hospital, Osaka University Hospital, Tokyo Women's Medical University Hospital, Mie University Hospital, Kansai Medical University Hirakata Hospital, Tohoku Rosai Hospital, Teikyo University Hospital, and Nara Medical University Hospital.

Definition of IF

The definition of IF in the present study was based on the proposed definition by the international consensus group [10]. CD patients who required intravenous infusion therapy at least twice per week for a period of more than 1 year because of inability to maintain protein-energy, fluid, electrolyte, or micronutrient balance, which resulted from surgical resection, were defined as having IF in the present study. Patients who received intravenous infusion therapy for bowel inflammation, bowel stenosis, fistula, abscess, and/or anal disease were excluded. In terms of the type of infusion fluid, both high-calorie fluid and crystalloid fluid were included in the study.

Patients and methods

A retrospective review of medical records from the 12 hospitals was conducted. CD patients who underwent initial intestinal surgery (bowel resection, strictureplasty, and/or stoma construction) at any of the 12 hospitals between January 1970 and December 2009 were collected ($n = 1{,}703$). Of the 1,703 patients, patients who developed IF by December 2010 were reviewed ($n = 68$), and the cumulative risk for developing IF after initial intestinal surgery was evaluated. In addition, CD patients with IF who underwent initial intestinal surgery at other hospitals and were then treated at any of the 12 hospitals were also reviewed ($n = 41$). Of the 41 patients, eight were excluded

Table 1 Number of CD/IF patients who underwent initial intestinal surgery at the 12 participating hospitals by decade

	Time of initial intestinal surgery				
	1970–1979	1980–1989	1990–1999	2000–2009	Total
CD patients	37	139	511	1,016	1,703
CD patients with IF	2 (5.4 %)	12 (8.6 %)	33 (6.5 %)	21 (2.1 %)	68 (4.0 %)

CD Crohn's disease, *IF* intestinal failure

from the present study because of insufficient clinical data. Hence, a total of 101 CD patients with IF were collected, and their characteristics were reviewed. The cumulative risk for IF-related death by the time from the occurrence of IF was evaluated.

The following clinical data were collected in patients with IF: age at diagnosis of CD, age at initial intestinal surgery, age at the occurrence of IF, age at the time of the study, number of surgeries to the occurrence of IF, bowel disease location, length of remnant small intestine at the occurrence of IF (which was evaluated by the findings at the surgery), medical therapies, and complications after the occurrence of IF.

Statistical analysis

The cumulative risks of IF after initial intestinal surgery and IF-related death by the time from the occurrence of IF were evaluated using the Kaplan–Meier method. CD patients without IF were regarded as censored cases. Quantitative and qualitative variables were compared using the Mann–Whitney U test. Values of $P < 0.05$ were considered significant. All statistical analyses were performed using SPSS® version 13.0J software (SPSS Japan, Tokyo, Japan).

Results

Cumulative risk of IF

A total of 1,703 CD patients underwent initial intestinal surgery at any of the 12 hospitals between 1970 and 2009 (Table 1). Of the 1,703 patients, 68 (4.0 %) developed IF. The cumulative risk for developing IF after the initial intestinal surgery was 0.8 % (5 years), 3.6 % (10 years), 6.1 % (15 years), and 8.5 % (20 years) (Fig. 1a).

In consideration of the historical bias, the cumulative risk of IF was also evaluated excluding 176 patients who underwent initial surgery between 1970 and 1989. A total of 1,527 CD patients underwent initial intestinal surgery at any of the 12 hospitals between 1990 and 2009. Of the 1,527 patients, 54 (3.5 %) developed IF. The cumulative risk of IF after the initial intestinal surgery was 0.6 % (5 years), 2.8 % (10 years), and 4.9 % (15 years) (Fig. 1b).

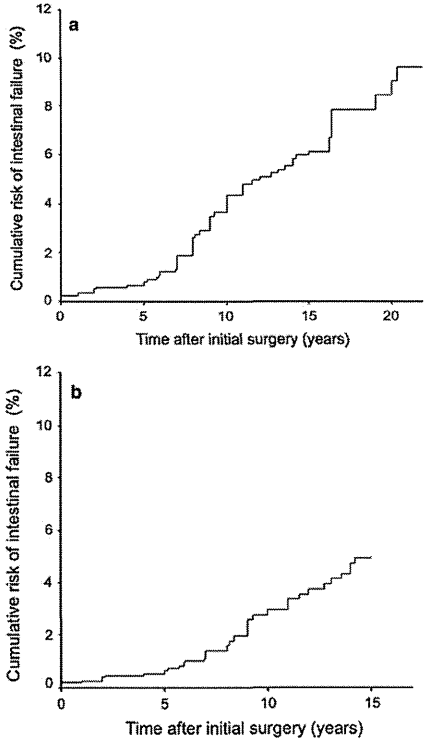

Fig. 1 Kaplan–Meier curve for the cumulative risk of intestinal failure in CD patients who underwent initial surgery between 1970 and 2009 ($n = 1,703$) (**a**) and between 1990 and 2009 ($n = 1,527$) (**b**)

Characteristics of CD patients with IF

The characteristics of the 101 CD patients with IF are shown in Table 2. The mean duration between CD diagnosis and the initial intestinal surgery was 6.4 years, and the mean duration between the initial surgery and the

Table 2 The characteristics of CD patients with IF ($n = 101$)

Age at (years)	
Diagnosis of CD	21.8 ± 8.8
Initial intestinal surgery	28.2 ± 9.3
Occurrence of IF	38.2 ± 10.7
Present (or age at death)	46.1 ± 11.4
No. of intestinal surgeries (times)	3.3 ± 1.7
Length of the small bowel (cm)	162 ± 64
Stoma	
Present (jejuno- or ileostomy/colostomy)	65 cases (64 %) (45/40)
Absent	36 (36 %)
Ileocecal valve	
Preserved	15 (15 %)
Resected	86 (85 %)

Mean ± SD

CD Crohn's disease, *IF* intestinal failure

Table 3 The characteristics of CD patients with IF who underwent initial surgery between 1990 and 2009 ($n = 63$)

Age at (years)	
Diagnosis of CD	21.1 ± 7.9
Initial intestinal surgery	29.1 ± 7.9
Occurrence of IF	35.8 ± 8.9
Present (or age at death)	42.0 ± 9.1
No. of intestinal surgeries (times)	3.1 ± 1.8
Length of the small bowel (cm)	176 ± 65
Stoma	
Present (jejuno- or ileostomy/colostomy)	46 cases (73 %) (36/10)
Absent	17 (27 %)
Ileocecal valve	
Preserved	8 (13 %)
Resected	55 (87 %)

Mean ± SD

CD Crohn's disease, *IF* intestinal failure

occurrence of IF was 10.0 years. The mean number of intestinal surgeries to the occurrence of IF was 3.3, and the mean length of remnant small intestine at the time of IF was 162 cm. The mean duration of follow-up after the occurrence of IF was 7.9 years. Sixty-five patients (64 %) had a stoma (jejuno- or ileostomy, $n = 45$; colostomy, $n = 20$), and 86 patients (86 %) had a resected ileocecal valve at the time of IF occurrence.

The characteristics of the 63 CD patients with IF who underwent initial surgery between 1990 and 2009 are shown in Table 3. Comparing the 38 CD patients with IF who underwent initial surgery before 1990, the mean length of remnant small intestine was significantly longer (176 vs. 138 cm, $P = 0.002$) and more patients had a stoma (73 vs. 50 %, $P = 0.022$).

Table 4 Medical treatments for CD patients with IF ($n = 101$)

	Before IF	After IF
HPN alone	–	4 cases (4 %)
5-ASA or sulphasalazine	76 cases (75 %)	74 (73 %)
Enteral nutrition	68 (67 %)	62 (61 %)
Steroid	48 (48 %)	28 (28 %)
Antimicrobial agent	29 (29 %)	31 (31 %)
Anti-TNF therapy	11 (11 %)	30 (30 %)
Immune-regulating agent	9 (9 %)	21 (21 %)
Cytapheresis	1 (1 %)	2 (2 %)
Intestinal surgery	101 cases	20 (20 %)
Unknown	11 cases	2 cases

CD Crohn's disease, *IF* intestinal failure, *HPN* home parenteral nutrition, *5-ASA* 5-aminosalicylic acid

Table 5 Medical treatments for CD patients with IF who underwent initial surgery between 1990 and 2009 ($n = 63$)

	Before IF	After IF
HPN alone	–	2 cases (3 %)
5-ASA or sulphasalazine	51 cases (81 %)	51 (81 %)
Enteral nutrition	44 (70 %)	41 (65 %)
Steroid	33 (52 %)	22 (35 %)
Antimicrobial agent	20 (32 %)	23 (37 %)
Anti-TNF therapy	7 (11 %)	21 (33 %)
Immune-regulating agent	5 (8 %)	12 (19 %)
Cytapheresis	1 (2 %)	1 (2 %)
Intestinal surgery	63 cases	13 (21 %)
Unknown	5 cases	1 cases

CD Crohn's disease, *IF* intestinal failure, *HPN* home parenteral nutrition, *5-ASA* 5-aminosalicylic acid

Medical treatments

The medical treatments for the CD patients with IF are shown in Table 4. Enteral nutrition was used in 68 patients (67 %) before the occurrence of IF and 62 patients (61 %) after the occurrence of IF. Twenty patients (20 %) underwent intestinal surgery during the mean 7.9 years of follow-up after the occurrence of IF. No patient underwent small bowel transplantation. The medical treatments for the CD patients with IF who underwent initial surgery between 1990 and 2009 are shown in Table 5. There were no significant differences in terms of medical treatment comparing the CD patients with IF who underwent initial surgery before 1990.

The intravenous infusion therapy given to the CD patients with IF is shown in Table 6. Excluding cases who died ($n = 12$) and weaned-off cases ($n = 16$), 73 IF

Table 6 Intravenous infusion therapy for CD patients with IF ($n = 73$)

Frequency of infusion (per week)	
7 times	58 cases (78 %)
4–6 times	4 (5 %)
3.5 times	7 (10 %)
2–3 times	4 (5 %)
Volume of infusion (per one time, mL)	
<1000	6 (8 %)
1000–2000	37 (51 %)
2000–3000	24 (33 %)
≥3000	6 (8 %)
Type of infusion	
High-calorie infusion	70 (96 %)
Crystalloid infusion	3 (4 %)

Excluding cases who died ($n = 12$) and weaned-off cases ($n = 16$), 73 IF patients were reviewed

patients were reviewed. Sixty-nine patients (95 %) used intravenous infusion therapy at least every second day, and 58 patients (79 %) used intravenous infusion every day. The median volume of infusion per time was 1500 mL. Seventy patients (96 %) used high-calorie infusion. The median number of calories by infusion was 1160 kcal/day.

Complications

Complications after the occurrence of IF are shown in Table 7. Seventy-nine patients (78 %) had at least one complication during the mean 7.9 years of follow-up after the occurrence of IF. Central venous catheter-related bloodstream infection (CRBSI) was the most frequent complication ($n = 58$, 57 %). Of the 58 patients, four died due to CRBSIs (Table 8). The frequency of CRBSI in CRBSI-related death cases ($n = 4$) was 2.4 times per 1000 days (mean), which was not significantly different from the other CRBSI cases ($n = 54$; 1.8 times per 1000 days) ($P = 0.636$). Liver dysfunction was the second most frequent complication ($n = 32$, 32 %).

Outcomes

The outcomes of CD patients with IF are shown in Table 8. Twelve patients (12 %) had died at 7.0 ± 4.0 years (mean ± SD) of follow-up after the occurrence of IF. The durations from the occurrence of IF to death were 4.5 ± 2.4 years (CRBSI), 7.4 ± 5.2 years (anorectal cancer), and 10.9 ± 4.5 years (liver cirrhosis). The ages at death were 37.5 ± 8.5 years (CRBSI), 59.4 ± 14.7 years (anorectal cancer), and 59.7 ± 14.6 years (liver cirrhosis). The cumulative risk of IF-related death (CRBSI or liver cirrhosis; $n = 6$) by the time from the occurrence of IF was

Table 7 Complications after the occurrence of IF ($n = 101$)

Complications			
Yes	79 cases (78 %)		
No	16 (16 %)		
Unknown	6 (6 %)		
CV catheter-related complication		Metabolic complication	
CRBSI	58 cases (57 %)	Liver dysfunction	32 cases (32 %)
Catheter obstruction	16 (16 %)	Mineral deficiency/excess	14 (14 %)
Loss of venous access	7 (7 %)	Vitamin B12 deficiency	12 (12 %)
Skin trouble at CV port	6 (6 %)	Renal dysfunction	12 (12 %)
CV port broken	4 (4 %)	Dehydration	11 (11 %)
Subcutaneous infection	3 (3 %)	Gall bladder stone	6 (6 %)
Infection		Renal stone	5 (5 %)
Infective endocarditis	2 (2 %)	Hyperuricemia	2 (2 %)
Fungal endophthalmitis	1 (1 %)	Electrolyte abnormality	2 (2 %)
Cerebral meningitis	1 (1 %)	Amyloidosis	1 (1 %)
Brain abscess	1 (1 %)	Growth disorder	1 (1 %)
Splenic abscess	1 (1 %)	Osteoporosis	1 (1 %)
Others		Renal anemia	1 (1 %)
Skin trouble	4 (4 %)		
Thrombosis	3 (3 %)		
GI hemorrhage	3 (3 %)		
Depression	2 (2 %)		

IF intestinal failure, *CV* central venous, *CRBSI* catheter-related bloodstream infection, *GI* gastrointestinal

1.1 % (3 years), 3.7 % (5 years), 6.5 % (7 years), and 8.9 % (10 years) (Fig. 2). Sixteen patients (16 %) were weaned from IF status after 4.1 ± 2.1 years from the occurrence of IF.

Discussion

The present study showed that the cumulative risk of IF in CD patients, who underwent initial intestinal surgery between 1970 and 2009, was less than 1 % at 5 years after the initial surgery, but the risk increased over 5 % at 15 years after the initial surgery. Because medical treatments and surgical techniques have changed, the authors also evaluated the risk of IF excluding patients who underwent initial surgery between 1970 and 1989 to avoid the historical bias. The cumulative risk of IF was still nearly 5 % at 15 years after the initial surgery. To the best of our

Table 8 Prognosis of CD patients with IF ($n = 101$)

Deaths	12 cases (12 %)
CRBSI	4 (4 %)
Anorectal cancer	4 (4 %)
Liver cirrhosis	2 (2 %)
Suicide	1 (1 %)
Intestinal perforation	1 (1 %)
Weaned off cases	16 (16 %)

CD Crohn's disease, *IF* intestinal failure, *CRBSI* catheter-related bloodstream infection

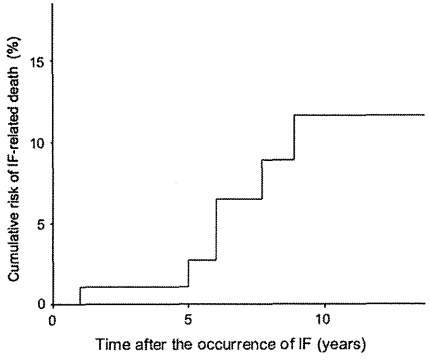

Fig. 2 Kaplan–Meier curve for the cumulative risk of IF-related death in CD patients with IF ($n = 101$)

knowledge, the present study is the first to estimate the cumulative risk for developing IF in patients with CD using the Kaplan–Meier method. To date, there has been a very limited number of studies concerning the incidence of IF in patients with CD. Most of these studies were population-based studies or small-sized studies, and they only assessed the incidence of IF at one time point [11–15]. Hurst et al. [13] reported that four (0.8 %) of 513 CD patients who underwent surgery between 1985 and 1996 developed IF, which was a short-term result, because the study was published in 1997. Dietz et al. [14] reported that 23 (10 %) of 219 CD patients developed IF at a median follow-up of 7.8 years after the initial operation. Yamamoto et al. [15] reported that two (4.5 %) of 44 CD patients developed IF at a median follow-up of 15 years after the initial operation. These studies support the present results; the occurrence of IF in CD patients is rare in the short-term period after initial surgery, though it is not rare over the long term.

In the present study, the term "intestinal failure (IF)" was used instead of the term "short bowel syndrome (SBS)" because the term "SBS" seems to indicate that the degree of malabsorption only depends on the length of the residual bowel itself [16]. However, both intestinal length and intestinal function affect the severity of malabsorption [17]. The term "IF" is a more general expression and refers directly to the intestinal function itself [16]. In CD patients, the intestinal absorptive function may be affected by the disease activity, as well as the bowel length; therefore, the present study used the term "IF" from the clinical standpoint. From the standpoint of intestinal length, in the present study, the mean length of remnant small intestine was 162 cm. The American Gastroenterological Association Clinical Practice Committee stated that SBS can occur when there is less than 200 cm of small bowel [10]. Hurst et al. [13] noted that 5 % of patients with CD were left with intestinal remnants of less than 180 cm after multiple resections, and were at risk for the development of SBS. These findings were consistent with the present study.

The present study showed that death was not rare in CD patients with IF. Several studies have reported that the overall 5-year mortality in HPN-treated patients (including CD and other diseases) ranged from 2 to 28 %, though most of these studies were population-based studies, and the precise mortality of CD patients with IF was still unclear [18–21]. To the best of our knowledge, the present study is the first to have estimated IF-related death in CD patients using the Kaplan–Meier method. The poor prognosis was mainly due to complications of HPN (CRBSI, liver dysfunction) and anorectal cancer. Since CRBSI and liver dysfunction were the most frequent complications in CD patients with IF, it is very important to prevent and/or manage these complications. In terms of CRBSI, previous studies reported that the occurrence rate of CRBSI in HPN patients (including CD and other diseases) ranged from 0.44 to 3 times per 1000 days [22–24]. The Center for Disease Control and Prevention (CDC) guideline recommended the use of a prophylactic antimicrobial lock solution in patients with long-term catheters who have a history of multiple CRBSIs despite optimal maximal adherence to aseptic technique [25]. In terms of liver dysfunction, parenteral nutrition–induced liver disease varies from steatosis due to excessive caloric administration to severe cholestatic injury with irreversible cirrhosis [26]. Optimal methods for preventing or retarding the development of liver dysfunction have not been established, although several have been proposed. A few recent studies indicated that substituting fish oil-based lipid solutions (rich in omega-3 fatty acids) may improve parenteral nutrition-associated cholestasis [27, 28]. Intestinal and/or liver transplantation is an option for some patients for whom other treatments have failed and who have complications from long-term parenteral nutrition. These patients are typically considered for transplantation as a result of the loss of venous access sites, recurrent and

persistent episodes of sepsis, and development of liver failure.

Finally, the limitations of the present study must be considered. Because the present study is a long-term study, there is a bias in terms of medical treatments. Recent studies showed that anti-TNF therapy was effective in maintaining remission in Crohn's disease [29, 30]and reduced the rate of surgery [31]. Another recent study showed that teduglutide, a glucagon-like peptide-2 (GLP-2) analogue, reduced volumes and numbers of days of parenteral support for SBS patients with IF (including CD and other diseases) [32]. There is a possibility that recent medical treatments including anti-TNF therapy and teduglutide reduce the occurrence of IF and/or prompts weaning from IF status in CD patients, though another long-term study is essential to clarify the issue. Similar to medical therapy, factors such as materials (e.g., central venous catheter) and infection countermeasures have changed over time. These factors may improve the managements of the IF patients and may reduce late complications, though further study is also needed to clarify the issue.

In conclusion, the present study showed that the incidence of IF in CD patients was not low over the long-term after initial surgery. CRBSI and liver dysfunction were the most frequent complications, and the poor prognosis was mainly due to these complications. To date, there are few treatments for SBS patients with IF [33]. There is a pressing need to develop strategies for the prevention and management of IF.

Acknowledgments The authors thank Hitoshi Ogawa and Sho Haneda (Tohoku University Hospital), Ken-ichi Takahashi (Tohoku Rosai Hospital), Daijiro Higashi (Fukuoka University Chikushi Hospital), Michio Itabashi and Shinpei Ogawa (Tokyo Women's Medical University), Toshimitsu Araki (Mie University Hospital), Keiji Matsuda (Teikyo University Hospital), Shinji Nakamura (Nara Medical University Hospital), Katsuyoshi Hatakeyama and Tsuneo Iiai (Nigata University Hospital), and Masahiko Watanabe (Kitasato University Hospital) for collecting data and/or important intellectual contributions.

Conflict of interest This work was supported in part by Health and Labour Sciences Research Grants for research on intractable diseases from the Ministry of Health, Labour and Welfare of Japan.

References

1. Vernier-Massouille G, Balde M, Salleron J, et al. Natural history of pediatric Crohn's disease: a population-based cohort study. Gastroenterology. 2008;135:1106–13.
2. Bernell O, Lapidus A, Hellers G. Risk factors for surgery and recurrence in 907 patients with primary ileocaecal Crohn's disease. Br J Surg. 2000;87:1697–701.
3. Bernell O, Lapidus A, Hellers G. Risk factors for surgery and postoperative recurrence in Crohn's disease. Ann Surg. 2000;231:38–45.
4. Basilisco G, Campanini M, Cesana B, et al. Risk factors for first operation in Crohn's disease. Am J Gastroenterol. 1989;84:749–52.
5. Peyrin-Biroulet L, Loftus EV Jr, Colombel JF, et al. The natural history of adult Crohn's disease in population-based cohorts. Am J Gastroenterol. 2010;105:289–97.
6. Williams J, Wong W, Rothenberger D, et al. Recurrence of Crohn's disease after resection. Br J Surg. 1991;78:10–9.
7. Greenstein AJ, Sachar DB, Pasternack BS, et al. Reoperation and recurrence in Crohn's colitis and ileocolitis Crude and cumulative rates. N Engl J Med. 1975;293:685–90.
8. Fleming CR, Remington M. Intestinal failure. In: Hill GL editor. Nutrition and the surgical patients. Clinical Surgery International. Edinburgh: Churchill Livingstone; 1981. p. 219–35.
9. Lal S, Teubner A, Shaffer JL. Review article: intestinal failure. Aliment Pharmacol Ther. 2006;24:19–31.
10. O'Keefe SJ, Buchman AL, Fishbein TM, et al. Short bowel syndrome and intestinal failure: consensus definitions and overview. Clin Gastroenterol Hepatol. 2006;4:6–10.
11. Mughal M, Irving M. Home parenteral nutrition in the United Kingdom and Ireland. Lancet. 1986;2:383–7.
12. Bakker H, Bozzetti F, Staun M, et al. Home parenteral nutrition in adults: a european multicentre survey in 1997. ESPEN-Home Artificial Nutrition Working Group. Clin Nutr. 1999;18:135–40.
13. Hurst RD, Molinari M, Chung TP, et al. Prospective study of the features, indications, and surgical treatment in 513 consecutive patients affected by Crohn's disease. Surgery. 1997;122:661–7.
14. Dietz DW, Fazio VW, Laureti S, et al. Strictureplasty in diffuse Crohn's jejunoileitis: safe and durable. Dis Colon Rectum. 2002;45:764–70.
15. Yamamoto T, Allan RN, Keighley MR. Long-term outcome of surgical management for diffuse jejunoileal Crohn's disease. Surgery. 2001;129:96–102.
16. Nordgaard I, Hansen BS, Mortensen PB. Importance of colonic support for energy absorption as small-bowel failure proceeds. Am J Clin Nutr. 1996;64:222–31.
17. Buchman AL, Scolapio J, Fryer J. AGA technical review on short bowel syndrome and intestinal transplantation. Gastroenterology. 2003;124:1111–34.
18. Messing B, Landais P, Goldfarb B, et al. Home parenteral nutrition for adults. Results of a multicenter survey in France. Presse Med. 1988;17:845–9.
19. Howard L, Ament M, Fleming CR, et al. Current use and clinical outcome of home parenteral and enteral nutrition therapies in the United States. Gastroenterology. 1995;109:355–65.
20. Silverberg MS, Satsangi J, Ahmad T, et al. Toward an integrated clinical, molecular and serological classification of inflammatory bowel disease: Report of a Working Party of the 2005 Montreal World Congress of Gastroenterology. Can J Gastroenterol. 2005;19 Suppl A:5–36.
21. Elriz K, Palascak-Juif V, Joly F, et al. Crohn's disease patients with chronic intestinal failure receiving long-term parenteral nutrition: a cross-national adult study. Aliment Pharmacol Ther. 2011;34:931–40.
22. Crispin A, Thul P, Arnold D, et al. Central venous catheter complications during home parenteral nutrition: a prospective pilot study of 481 patients with more than 30,000 catheter days. Onkologie. 2008;31:605–9.
23. Ireton-Jones C, DeLegge M. Home parenteral nutrition registry: a five-year retrospective evaluation of outcomes of patients receiving home parenteral nutrition support. Nutrition. 2005;21:156–60.
24. Reimund JM, Arondel Y, Finck G, et al. Catheter-related infection in patients on home parenteral nutrition: results of a prospective survey. Clin Nutr. 2002;21:33–8.
25. O'Grady NP, Alexander M, Burns LA, et al. Guidelines for the prevention of intravascular catheter-related infections. Am J Infect Control. 2011;39(Suppl 1):S1–34.

26. Vanderhoof JA, Langnas AN. Short-bowel syndrome in children and adults. Gastroenterology. 1997;113:1767–78.
27. Gura KM, Duggan CP, Collier SB, et al. Reversal of parenteral nutrition-associated liver disease in two infants with short bowel syndrome using parenteral fish oil: implications for future management. Pediatrics. 2006;118:197–201.
28. Gura KM, Lee S, Valim C, et al. Safety and efficacy of a fish-oil-based fat emulsion in the treatment of parenteral nutrition-associated liver disease. Pediatrics. 2008;121:678–86.
29. Yoshida K, Fukunaga K, Ikeuchi H, et al. Scheduled infliximab monotherapy to prevent recurrence of Crohn's disease following ileocolic or ileal resection: a 3-year prospective randomized open trial. Inflamm Bowel Dis. 2012;18:1617–23.
30. Colombel JF, Sandborn WJ, Reinisch W, et al. Infliximab, azathioprine, or combination therapy for Crohn's disease. N Engl J Med. 2010;362:1383–95.
31. Lichtenstein GR, Yan S, Bala M, et al. Infliximab maintenance treatment reduces hospitalizations, surgeries, and procedures in fistulizing Crohn's disease. Gastroenterology. 2005;128:862–9.
32. Jeppesen PB, Pertkiewicz M, Messing B, et al. Teduglutide reduces need for parenteral support among patients with short bowel syndrome with intestinal failure. Gastroenterology. 2012;143:1473–81.
33. Buchman AL. Teduglutide and short bowel syndrome: every night without parenteral fluids is a good night. Gastroenterology. 2012;143:1416–20.